Journal of Computational Physics 228 (2009) 1234–1274

Contents lists available at ScienceDirect

Journal of Computational Physics

journal homepage: www.elsevier.com/locate/jcp

The MAST FV/FE scheme for the simulation of two-dimensional thermohaline processes in variable-density saturated porous media

Costanza Aricò *, Tullio Tucciarelli

Dipartimento di Ingegneria Idraulica ed Applicazioni Ambientali, Università di Palermo Viale delle Scienze, 90128 Palermo, Italy

ARTICLE INFO

Article history:
Received 9 May 2008
Received in revised form 29 September 2008
Accepted 15 October 2008
Available online 1 November 2008

Keywords:
Density driven flows
Thermohaline process
Finite volume method
Finite element method
Porous media
Stream function

ABSTRACT

A novel methodology for the simulation of 2D thermohaline double diffusive processes, driven by heterogeneous temperature and concentration fields in variable-density saturated porous media, is presented. The stream function is used to describe the flow field and it is defined in terms of mass flux. The partial differential equations governing system is given by the mass conservation equation of the fluid phase written in terms of the mass-based stream function, as well as by the advection–diffusion transport equations of the contaminant concentration and of the heat. The unknown variables are the stream function, the contaminant concentration and the temperature. The governing equations system is solved using a fractional time step procedure, splitting the convective components from the diffusive ones. In the case of existing scalar potential of the flow field, the convective components are solved using a finite volume marching in space and time (MAST) procedure; this solves a sequence of small systems of ordinary differential equations, one for each computational cell, according to the decreasing value of the scalar potential. In the case of variable-density groundwater transport problem, where a scalar potential of the flow field does not exist, a second MAST procedure has to be applied to solve again the ODEs according to the increasing value of a new function, called approximated potential. The diffusive components are solved using a standard Galerkin finite element method. The numerical scheme is validated using literature tests.

1. Introduction

A number of environmental problems require the study of transport dynamics in subsurface systems, e.g. disposal of hazardous, infiltration of leachates from landfills and industrial waste disposals, seawater intrusion in coastal aquifers.

Most of the hydrogeological studies have been addressed in the past of groundwater saturated flow problems by assuming a constant-density of the water and the flow as being driven by pressure differences only. These assumptions imply the existence of a scalar potential of the velocity field, allowing several analytical solutions.

With the growing interest in the simulation of hydrogeological processes involved in the management of natural resources, it has been recognized that the assumption of constant water density is no longer adequate for the simulation of flow fields in the above mentioned cases.

Thermohaline processes are connected with the presence of heterogeneous temperature and concentration fields and convective currents arise from heat and salinity gradients acting simultaneously. Groundwater density may vary as result of either pressure, either pollutant/salt concentration, either temperature variations. Density differences produce convective

* Corresponding author. Tel.: +39 091 6657773; fax: +39 091 6657749.
E-mail addresses: arico@idra.unipa.it (C. Aricò), tucciar@idra.unipa.it (T. Tucciarelli).

0021-9991/$ - see front matter © 2008 Elsevier Inc. All rights reserved.
doi:10.1016/j.jcp.2008.10.015

currents and density gradients introduce gravitational instabilities that give rise to recirculating groundwater systems. Such phenomena are usually indicated as *density driven* flows.

The partial differential equations (PDEs) governing system is given by the mass conservation equation of the fluid phase, by the Darcy formula for the velocity and by the advection–dispersion transport equations of the heat and the contaminant solute.

In the past decades, finite-differences (FD) and finite element (FE) methods have been widely employed to solve the nonlinear coupled balance equations for variable-density groundwater problems [16]. FE methods based on the primitive variables fluid pressure and flow velocity components have been proposed and used by Segol et al. [48], Huyakorn and Taylor [33] and Diersch [13,14].

Because the Darcy flux is embedded in the continuity equation as function of the spatial gradient of the piezometric head h, a careful handling of the derivative terms is required. The use of only piecewise continuous basis functions for h generate velocity fields with discontinuities across elements boundaries. In this case, according to Diersch and Kolditz [16], the nonunique value of the velocity across the element boundary could generate spurious vertical velocity components due to the inappropriate balance approximation of the lower order term (∇h), constant inside the element when using linear basis functions, and the higher order gravitational buoyancy term, varying linearly inside the element assuming the same basis functions for concentration and temperature.

Several techniques have been proposed to circumvent this problem. Voss and Souza [53] used in 2D a reduced-order approximation of the buoyancy terms. Averaging the concentration inside each element, the pressure gradients and the concentration distribution are constant in space when linear basis functions are used. Herbert et al. [31] introduced a mixed interpolation strategy in the NAMMU 2D code, where pressure is approximated by quadratic elements to obtain linearly distributed pressure gradients which becomes consistent with linear distribution of the concentration-dependent buoyancy term.

Many numerical methods proposed in literature originate from the splitting of the advective flux components from the diffusive ones into different PDEs containing separately the advective and the diffusive terms. The PDEs are discritized in space and time, each with the technique deemed most appropriate. Most often, explicit time-stepping for advective fluxes are combined with implicit time-stepping for dispersive/diffusive fluxes. Eulerian–Lagrangian schemes [7,42] and Eulerian–Godunov schemes [8–11] belong to these kinds of splitting methods.

For the advective components of the transport equation some authors (see for example [37–39]) adopt high resolution triangular finite volume (FV) discretization, combined with an implicit mixed hybrid finite element (MHFE) scheme for the solution of the flow equation and of the diffusive components in the transport equation. MHFE methods compute a velocity field which is very good for the solution of the next convective transport problem with the FV methods, since the normal velocity components are continuous across the inter-element boundaries. This avoids mass balance errors in the solution of the transport equations due to inaccuracies in the evaluation of the fluxes through the element interfaces. In addition, the use of a dual mesh for the FV scheme is no necessary if a MHFE method is applied for the discretization of the diffusive components.

Because of the explicit time discretization, most often the solution of the advective components is limited by the courant (CFL) stability requirement on the size of the time step, while, because of the implicit time discretization, there is no restriction on the time step of the MHFE. This implies that different time steps are used for the solution of the advection and of the diffusion problems. Solution of the advective components is carried out by applying na times the FV scheme using a time step size $\Delta ta = \Delta t/na$. Values of na and Δta vary inside the computational domain according to the CFL restriction.

In the present paper, a novel methodology for the simulation of 2D thermohaline double diffusive processes, with heterogeneous temperature and concentration fields in variable-density saturated porous media, is presented.

The governing equations system is solved applying a fractional time step procedure, by means of a mixed finite volume/finite element method (FV/FE). The inviscid terms of the problem are discretized by means of a marching in space and time (MAST) scheme. This is a Finite Volume scheme, recently proposed for the solution of the fully dynamic 1D and 2D shallow water equations [3,4,41,43,51] as well as for the solution of convection dominated problems [2,5]. MAST is particularly suitable for the solution of inviscid flows because it allows a direct solution of entirely convective problems and has shown unconditional stability with regard to the time step size. The viscous terms of the problems are discretized by means of a standard Galerkin piece-wise linear finite element method, which allows a careful reconstruction of head spatial gradients on irregular domain. Because of the unconditional stability with regard to the time step size, iterative procedure for the solution of the advective components is not necessary in the proposed procedure and the same constant time step is used for both the FV and FE schemes.

The extension of the proposed MAST FV/FE procedure to the general 3D case, without the help of the stream function for the velocity field estimation, is finally outlined.

2. Physical model assumptions and governing equations system

The medium is assumed to be saturated with a single liquid phase, composed of N_s miscible chemical species, with density ρ_k and concentration C_k, $k = 1,\ldots,N_s$. In the following, only one chemical soluble specie is assumed ($k = N_s = 1$).

The governing equations for the coupled mass and heat transport in saturated porous media form a partial differential equations (PDEs) non-linear system given by the flow equation as well as by the transport equations of the contaminant phase and of the heat [19].

The system is assumed to be symmetrical with respect to any vertical plane, with directions x_1 (horizontal) and x_2 (vertical). Due to this simplification, the 2D assumption is made and the flow equation is formulated in terms of mass-based stream function [22].

Generally, continuity equation of the liquid phase can be written as

$$\nabla \cdot (\rho \mathbf{q}) = 0, \tag{1}$$

where ρ is the fluid density and $\mathbf{q}$ is the Darcy velocity whose components along $x_1 = x$ and $x_2 = z$ directions are q_{x_1} and q_{x_2}.

The general form of the Darcy's law for variable-density conditions is [6]:

$$\mathbf{q} = -\frac{\mathbf{k}}{\mu}(\nabla p + \rho g \nabla x_2), \tag{2}$$

where $\mathbf{k}$ is the permeability tensor, μ is the fluid viscosity, p is the fluid pressure, g is the gravitational acceleration and x_2 is the upward coordinate aligned with gravity. Using freshwater as reference fluid, the equivalent freshwater head can be defined as

$$h = \frac{p}{\rho_0 g} + x_2, \tag{3}$$

where ρ_0 is the freshwater density and the Darcy's law in Eq. (2) becomes:

$$\mathbf{q} = -\frac{\mathbf{k}}{\mu}(\rho_0 g \nabla h + (\rho - \rho_0) g \nabla x_2). \tag{4}$$

According to Eq. (4), fluid flow is caused by two driving forces: the piezometric head difference (where the head is referred to a fictitious fluid with density ρ_0) and the buoyancy force acting on a fluid of density ρ imbedded in a fluid with density ρ_0.

In cases of constant-density flow problems, the hydraulic head is a potential function that completely describes the flow field; equipotentials are everywhere normal to the flow lines and the stream function and the hydraulic head satisfy the Cauchy–Riemann conditions [6].

In variable-density groundwater problems, flow is not described by a potential function. In these cases the stream function relates flow directly to vorticity arising from lateral density gradient [12]. Call Ψ the scalar function "*mass-based stream function*" describing the flow field [22]:

$$\begin{cases} \rho q_{x_1} = -\frac{\partial \Psi}{\partial x_2} \\ \rho q_{x_2} = \frac{\partial \Psi}{\partial x_1} \end{cases} \Rightarrow \begin{cases} q_{x_1} = -\frac{1}{\rho}\frac{\partial \Psi}{\partial x_2} \\ q_{x_2} = \frac{1}{\rho}\frac{\partial \Psi}{\partial x_1} \end{cases}. \tag{5}$$

By substituting the Darcy's law into the continuity Eq. (1), after some manipulations one gets [22]:

$$\nabla \cdot \left(\frac{\mathbf{K}}{|\mathbf{K}|} \frac{1}{\rho \mu_r} \cdot \nabla \Psi \right) = -\frac{\partial \rho_r}{\partial x_1}, \tag{6}$$

where $\mathbf{K} = \mathbf{k}\rho_0 g/\mu_0$ is the freshwater hydraulic conductivity tensor, $\mu_r = \mu_0/\mu$ is the relative viscosity, μ_0 is the reference freshwater viscosity and $\rho_r = (\rho - \rho_0)/\rho_0$ is the relative density.

The use of the stream function implies steady-state flow or negligible storage changes. While this is not a severe assumption in free convection problems, it could become inappropriate for the simulation of transient flow near pumping wells. Another disadvantage in the use of the stream function formulation is the difficulty in specifying internal heat, pollutant and fluid sources and/or sinks, owing to consequent discontinuities in Ψ [22].

On the other hand, the use of the stream function allows a more precise estimation of the flow field, that should be otherwise estimated by means of Eq. (2), where the two terms in the brackets have different approximation order [16].

The transport equation for pollutant and heat are given by [16,17,25]:

$$\frac{\partial(\varepsilon C)}{\partial t} + \nabla \cdot (\mathbf{q} C) - \nabla \cdot (\mathbf{D} \cdot \nabla C) = Q_C, \tag{7}$$

where C is the mass concentration of the solute component, Q_C is the sink/source of the solute component and $\mathbf{D}$ is the tensor of hydrodynamic dispersion. Similarly, the heat transport equation can be written as

$$\frac{\partial((\varepsilon \rho c^l + (1-\varepsilon)\rho^s c^s)T)}{\partial t} + \rho c^l \nabla \cdot (\mathbf{q} T) - \nabla \cdot (\mathbf{\Lambda} \cdot \nabla T) = Q_T, \tag{8}$$

where T is the temperature, ρ^s is the solid phase density, ρc^l and $\rho^s c^s$ are the thermal capacity of the fluid and the solid respectively (assumed constant in space and time), Q_T is the sink/source of the heat and $\mathbf{\Lambda}$ is the tensor of the hydrodynamic–thermo-dispersion. In deriving Eq. (8), equilibrium between liquid and solid temperature has been assumed.

The PDEs governing system is given by the flow Eq. (6) and by the transport equation for pollutant and heat (Eqs. (7) and (8)).

To close the set of the governing equations the following constitutive relationships are needed:

(1) The equation of state (EOS), defining the dependence of the fluid density on the pollutant concentration and on the temperature [16,17]:

$$\rho = \rho_0\left(1 + \frac{\bar{\alpha}}{(C_s - C_0)}(C - C_0) - \bar{\beta}(T - T_0)\right), \tag{9}$$

where $\bar{\alpha}$ is the fluid density difference ratio, C_s is the maximum concentration value, $\bar{\beta}$ is the fluid expansion coefficient and sub-index 0 indicates the reference values of concentration and temperature;

(2) The tensor of hydrodynamic dispersion **D**, given by [16,17]:

$$\mathbf{D} = (\varepsilon D_d + \beta_T|\mathbf{q}|)\mathbf{I} + (\beta_L - \beta_T)\frac{\mathbf{q}\otimes\mathbf{q}}{|\mathbf{q}|}, \tag{10}$$

where D_d is the molecular diffusion coefficient of the fluid, β_L and β_T are the longitudinal and transverse coefficients of the solute dispersivity, $|\mathbf{q}|$ is the absolute specific Darcy fluid flux and δ_{ij} is equal to 1 if $i = j$, otherwise it is equal to zero;

(3) The tensor of the hydrodynamic–thermo-dispersion $\mathbf{\Lambda}$, given by [16,17]:

$$\mathbf{\Lambda} = \mathbf{\Lambda}^{cond} + \mathbf{\Lambda}^{disp}, \quad \mathbf{\Lambda}^{cond} = (\varepsilon\lambda^l + (1-\varepsilon)\lambda^s)\mathbf{I}, \quad \mathbf{\Lambda}^{disp} = \rho c^l\left(\alpha_T|\mathbf{q}|\mathbf{I} + (\alpha_L - \alpha_T)\frac{\mathbf{q}\otimes\mathbf{q}}{|\mathbf{q}|}\right), \tag{11}$$

where λ^l and λ^s are respectively the thermal conductivity of the liquid and solid phase and α_L and α_T are the longitudinal and transverse thermodispersivity coefficients of the liquid phase;

(4) The liquid viscosity μ, function of the pollutant concentration and of the temperature, as further specified.

The mass conservation equation for the liquid phase (Eq. (1)) leads to:

$$\nabla\cdot\mathbf{q} = -\frac{\mathbf{q}\cdot\nabla\rho}{\rho}, \tag{12a}$$

and according to the EOS, Eq. (12a) can be written in the following form:

$$\nabla\cdot\mathbf{q} = -\mathbf{q}\frac{\rho_0}{\rho}\cdot\left(\frac{\bar{\alpha}}{C_s - C_0}\nabla C - \bar{\beta}\nabla T\right). \tag{12b}$$

Substituting the divergent terms in the conservation Eqs. (7) and (8), one gets:

$$\varepsilon\frac{\partial C}{\partial t} + \left(1 - \frac{\bar{\alpha}}{C_s - C_0}C\frac{\rho_0}{\rho}\right)\mathbf{q}\cdot\nabla C + \bar{\beta}C\frac{\rho_0}{\rho}\mathbf{q}\cdot\nabla T - \nabla\cdot(\mathbf{D}\cdot\nabla C) = Q_C, \tag{13}$$

$$(\varepsilon\rho c^l + (1-\varepsilon)\rho^s c^s)\frac{\partial T}{\partial t} + \rho c^l\left(1 + \bar{\beta}T\frac{\rho_0}{\rho}\right)\cdot\mathbf{q}\cdot\nabla T - \rho c^l\left(\frac{\bar{\alpha}}{C_s - C_0}T\frac{\rho_0}{\rho}\right)\cdot\mathbf{q}\cdot\nabla C - \nabla\cdot(\mathbf{\Lambda}\cdot\nabla T) = Q_T, \tag{14}$$

where porosity changes in time have been assumed to be negligible.

The difficulties in managing internal sinks/sources when fluid mass continuity equation is formulated in terms of stream function, mentioned before, can be circumvented by considering the source point as an external boundary (see Fig. 1(b) as opposite to Fig. 1(a)) and by modifying the boundary conditions. Similarly, in the pollutant and heat transport equations the sink/source points are treated as external boundary, properly changing the boundary conditions and the source terms on the r.h.s. of Eqs. (13) and (14). Finally, the PDEs governing system can be written as

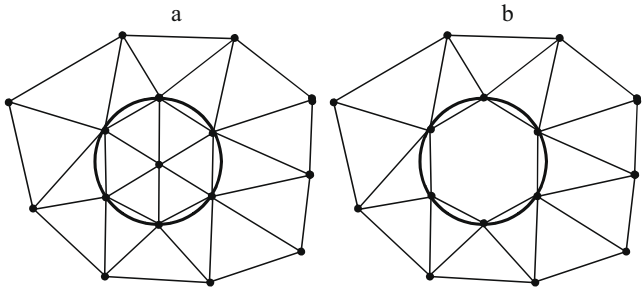

Fig. 1. FE representation of an injection (abstraction well) as (a) distributed source (sink); (b) external boundary (adapted from [25]).

$$\nabla\cdot\left(\frac{\mathbf{K}}{|\mathbf{K}|}\frac{1}{\rho\mu_r}\cdot\nabla\Psi\right)=-\frac{\partial\rho_r}{\partial x_1},$$
$$\varepsilon\frac{\partial C}{\partial t}+\left(1-\frac{\bar{\alpha}}{C_s-C_0}C\frac{\rho_0}{\rho}\right)\mathbf{q}\cdot\nabla C+\bar{\beta}C\frac{\rho_0}{\rho}\mathbf{q}\cdot\nabla T-\nabla\cdot(\mathbf{D}\cdot\nabla C)=0,$$
$$(\varepsilon\rho c^l+(1-\varepsilon)\rho^s c^s)\frac{\partial T}{\partial t}+\rho c^l\left(1+\bar{\beta}T\frac{\rho_0}{\rho}\right)\cdot\mathbf{q}\cdot\nabla T-\rho c^l\left(\frac{\bar{\alpha}}{C_s-C_0}T\frac{\rho_0}{\rho}\right)\cdot\mathbf{q}\cdot\nabla C-\nabla\cdot(\mathbf{\Lambda}\cdot\nabla T)=0. \tag{15}$$

3. A mixed FV/FE method for the solution of the PDEs governing system

3.1. Dual finite volume mesh

Discretization of system (15) is carried out on a generally unstructured triangular mesh. Let $\Omega\subset\Re^2$ be a bounded domain, Ω_h a polygonal approximation of Ω and T_h an unstructured Delaunay-type triangulation of Ω_h. The triangulation T_h is called *basic mesh* and the triangle e_T is called *primary element*. Let $P_h=\{P_i,\ i=1,\ldots,J\}$ the set of all vertices of all $e_T\in T_h$ and J a suitable index set. The *dual mesh* $E_h=\{e_i,\ i=1,\ldots,J\}$ is constructed over the basic mesh. The dual finite volume e_i associated with the vertex P_i is the closed polygon given by the union of sub-triangles resulting from the subdivision of each triangle of T_h connected to node P_i by means of its axes (see Fig. 2). In the following of the paper the dual volumes e are called also cells. The sub-triangles are called *secondary elements* and are indicated as e^{II}. Cells e_i satisfy:

$$\Omega=\cup e_i. \tag{16}$$

The boundary of e_i is denoted as ∂e_i and the outward normal unit vector to ∂e_i is denoted as n (see Fig. 2). The cells satisfy:

$$e_i\cap e_j=\{\mathbf{x}:\mathbf{x}\in\partial e_i\quad\text{and}\quad\mathbf{x}\in\partial e_j\}. \tag{17}$$

The choice of the centre of axes instead of the centre of gravity of each triangle is motivated in Appendix 1.

3.2. Integral form of the PDEs governing system

3.2.1. The case of constant-density groundwater transport problem

We derive first the proposed numerical procedure for a constant-density $\rho=\rho_0$ groundwater flow problem, where, as previously specified, a scalar potential function given by the hydraulic head completely describes the flow field. In this case, the continuity Eq. (1) simplifies in the following one:

$$\nabla\cdot\mathbf{q}=0, \tag{18}$$

The continuity Eq. (6) expressed in terms of stream function Ψ becomes a classical Laplace equation with zero source term:

$$\nabla\cdot\left(\frac{\mathbf{K}}{|\mathbf{K}|}\nabla\Psi\right)=0. \tag{19}$$

Assume a general system of balance laws:

$$\frac{\partial\mathbf{U}}{\partial t}+\nabla\cdot\mathbf{F}(\mathbf{U})=\mathbf{B}(\mathbf{U})+\nabla\cdot\mathbf{R}(\mathbf{U}), \tag{20}$$

where $\mathbf{U}$ is the vector of the unknown variables, $\mathbf{F}(\mathbf{U})$ represents the convective flux term vector, $\mathbf{B}(\mathbf{U})$ is the source term and $\mathbf{R}(\mathbf{U})$ represents the diffusive fluxes. Applying a fractional time step procedure to system (20), we set:

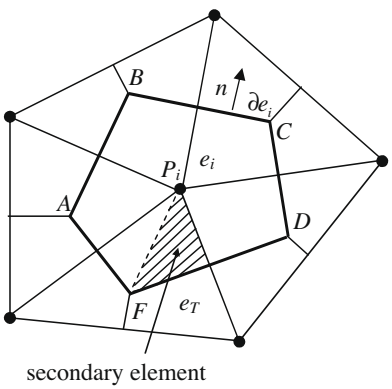

Fig. 2. The basic mesh and the dual finite volume mesh.

$$\begin{aligned}\mathbf{F}(\mathbf{U}) &= \mathbf{F}^p(\mathbf{U}) + (\mathbf{F}(\mathbf{U}) - \mathbf{F}^p(\mathbf{U})),\\ \mathbf{B}(\mathbf{U}) &= \mathbf{B}^p(\mathbf{U}) + (\mathbf{B}(\mathbf{U}) - \mathbf{B}^p(\mathbf{U})),\\ \mathbf{R}(\mathbf{U}) &= \mathbf{R}^p(\mathbf{U}) + (\mathbf{R}(\mathbf{U}) - \mathbf{R}^p(\mathbf{U})).\end{aligned} \tag{21}$$

where $\mathbf{F}^p(\mathbf{U})$, $\mathbf{B}^p(\mathbf{U})$ and $\mathbf{R}^p(\mathbf{U})$ are, respectively a suitable numerical convective flux term, source term and diffusive flux term, further defined.

After integration in time, system (20) can be split in the two following ones:

$$\mathbf{U}^{k+1/2} - \mathbf{U}^k + \nabla \cdot \int_0^{\Delta t} \mathbf{F}^p dt = \int_0^{\Delta t} \mathbf{B}^p dt + \nabla \cdot \int_0^{\Delta t} \mathbf{R}^p dt, \tag{22a}$$

$$\mathbf{U}^{k+1} - \mathbf{U}^{k+1/2} + \nabla \cdot \int_0^{\Delta t} \mathbf{F} dt - \nabla \cdot \overline{\mathbf{F}}^p = \int_0^{\Delta t} \mathbf{B} dt - \overline{\mathbf{B}}^p + \nabla \cdot \int_0^{\Delta t} \mathbf{R} dt - \nabla \cdot \overline{\mathbf{R}}^p, \tag{22b}$$

we call systems (22a and b) prediction and correction systems, respectively and $\overline{\mathbf{F}}^p$, $\overline{\mathbf{B}}^p$ and $\overline{\mathbf{R}}^p$ are the mean values of the numerical convective flux, source and diffusive flux terms computed during the prediction step; $\mathbf{U}^{k+1}$ and $\mathbf{U}^{k+1/2}$ are the unknown variables computed respectively at the end of the prediction and the correction phase. Observe that summing systems (22a and b), the integral of the original system (20) is formally obtained. The numerical corrected solution will be close to the one of the original system (20) as far as the difference between the predicted and original convective and diffusive fluxes and source terms is either small or time-independent. The advantage of using formulation (22) instead of (20) is that, with a suitable choice of the prediction terms $\mathbf{F}^p(\mathbf{U})$, $\mathbf{B}^p(\mathbf{U})$ and $\mathbf{R}^p(\mathbf{U})$, each of the two systems (22a and b) can be much easier to solve than the original system (20).

For the transport of pollutant and heat in a constant-density groundwater field, we set:

$$\mathbf{U} = (\,\Psi \quad C \quad T\,)^T, \tag{23a}$$

$$\begin{aligned}\mathbf{F} &= \begin{pmatrix} 0 \\ \frac{1}{\varepsilon}\mathbf{q}C \\ \frac{\rho c^l}{\varepsilon\rho c^l + (1-\varepsilon)\rho^s c^s}\mathbf{q}T \end{pmatrix}, \quad \mathbf{F}^p = \begin{pmatrix} 0 \\ \frac{1}{\varepsilon}\mathbf{q}^k C \\ \frac{\rho c^l}{\varepsilon\rho c^l + (1-\varepsilon)\rho^s c^s}\mathbf{q}^k T \end{pmatrix},\\ \mathbf{B} &= \begin{pmatrix} 0 \\ 0 \\ 0 \end{pmatrix}, \quad \mathbf{B}^p = \begin{pmatrix} 0 \\ (\mathbf{D}\cdot\nabla C)^k \\ (\mathbf{\Lambda}\cdot\nabla T)^k \end{pmatrix}, \quad \mathbf{R} = \begin{pmatrix} -\frac{\mathbf{K}}{|\mathbf{K}|}\cdot\nabla\Psi \\ \mathbf{D}\cdot\nabla C \\ \mathbf{\Lambda}\cdot\nabla T \end{pmatrix}, \quad \mathbf{R}^p = \begin{pmatrix} 0 \\ 0 \\ 0 \end{pmatrix},\end{aligned} \tag{23b}$$

in the prediction step we assume the flow velocity field as function of the gradients of Ψ computed at the end of the previous time step:

$$q_{x_1} = -\frac{1}{\rho_0}\frac{\partial \Psi^k}{\partial x_2}, \quad q_{x_2} = \frac{1}{\rho_0}\frac{\partial \Psi^k}{\partial x_1}. \tag{24}$$

The velocity is assumed constant during the given time step; the argument of the integral prediction system (22a) can be written as

$$\varepsilon\frac{\partial C}{\partial t} + \mathbf{q}\cdot\nabla C = \nabla\cdot(\mathbf{D}\cdot\nabla C)^k, (\varepsilon\rho c^l + (1-\varepsilon)\rho^s c^s)\frac{\partial T}{\partial t} + \rho c^l \mathbf{q}\cdot\nabla T = \nabla\cdot(\mathbf{\Lambda}\cdot\nabla T)^k \tag{25}$$

where the equation corresponding to the liquid continuity equation changes into an identity. Observe that the two equations in system (25) differ from the original one (15) in the time level of the gradients of Ψ in the expression of velocity in Eq. (24) and of the diffusive fluxes.

The argument of the integral correction system (22b) can be written as

$$\begin{aligned}&\nabla\cdot\left(\left(\frac{\mathbf{K}}{|\mathbf{K}|}\right)^{k+1/2}\cdot\nabla\Psi\right) = 0, \varepsilon\frac{\partial C}{\partial t} - \nabla\cdot(\mathbf{D}^{k+1/2}\cdot\nabla C) = -\nabla\cdot(\mathbf{D}\cdot\nabla C)^k\\ &(\varepsilon\rho c^l + (1-\varepsilon)\rho^s c^s)\frac{\partial T}{\partial t} - \nabla\cdot(\mathbf{\Lambda}^{k+1/2}\cdot\nabla T) = -\nabla\cdot(\mathbf{\Lambda}\cdot\nabla T)^k,\end{aligned} \tag{26}$$

where the index $k+1/2$ indicates the values computed at the end of the prediction step.

Observe that in the second and third Eq. (26), the difference between the pollutant and heat convective fluxes and their corresponding mean values computed during the prediction phase is neglected. Observe also that system (26) has been linearized assuming the values of both tensors $\mathbf{D}$ and $\mathbf{\Lambda}$ as well as the value of the term $\left(\frac{\mathbf{K}}{|\mathbf{K}|}\right)$ equal to the ones computed at the end of the prediction step.

After simple manipulations, systems (25) can be written in quasi-linear form as

$$\frac{\partial \mathbf{U}}{\partial t} + \mathbf{A}_1^{x_1}\begin{pmatrix} \frac{\partial\Psi}{\partial x_1} \\ \frac{\partial C}{\partial x_1} \\ \frac{\partial T}{\partial x_1} \end{pmatrix} + \mathbf{A}_1^{x_2}\begin{pmatrix} \frac{\partial\Psi}{\partial x_2} \\ \frac{\partial C}{\partial x_2} \\ \frac{\partial T}{\partial x_2} \end{pmatrix} = \begin{pmatrix} 0 \\ \nabla\cdot(\mathbf{D}\cdot\nabla C)^k \\ \nabla\cdot(\mathbf{\Lambda}\cdot\nabla T)^k \end{pmatrix}, \tag{27}$$

where matrices $\mathbf{A}_1^{x_1}$ and $\mathbf{A}_1^{x_2}$ are given by

$$\mathbf{A}_1^{x_1} = \begin{pmatrix} 0 & 0 & 0 \\ 0 & \frac{1}{\varepsilon} q_{x_1} & 0 \\ 0 & 0 & \frac{1}{(\varepsilon\rho c^l + (1-\varepsilon)\rho^s c^s)} q_{x_1} \rho c^l \end{pmatrix} \quad \text{and} \quad \mathbf{A}_1^{x_2} = \begin{pmatrix} 0 & 0 & 0 \\ 0 & \frac{1}{\varepsilon} q_{x_2} & 0 \\ 0 & 0 & \frac{1}{(\varepsilon\rho c^l + (1-\varepsilon)\rho^s c^s)} q_{x_2} \rho c^l \end{pmatrix}. \tag{28}$$

It is easy to show that the eigenvalues of matrices $\mathbf{A}_1^{x_1}$ and $\mathbf{A}_1^{x_2}$ are $\lambda_1 = 0$, $\lambda_2 = \frac{1}{\varepsilon} q_{x_1(x_2)}$ and $\lambda_3 = \frac{1}{(\varepsilon\rho c^l + (1-\varepsilon)\rho^s c^s)} q_{x_1(x_2)} \rho c^l$; this implies that the first eigenvalue is zero and the sign of the second and the third one is always the same of the corresponding velocity components; the solution of system (25) is equivalent to the solution of a single non-linear convection equation, function of the gradient of the stream function at time level t^k, while system (26) has the functional characteristics of a pure diffusive process. For these reasons we call the prediction and the correction systems, respectively convective prediction system and diffusive correction system.

We solve the prediction step using a FV procedure and the diffusive step using a FE formulation.

For the prediction step, we assume a first spatial approximation order (piecewise constant) of variables C and T inside each cell.

The convective volume concentration and heat fluxes through the jth side of the dual volume e are given by

$$FL^e_{C,j} = C_e[q^{e^{II,j}}_{x_1}(x^e_{2,jp} - x^e_{2,j}) - q^{e^{II,j}}_{x_2}(x^e_{1,jp} - x^e_{1,j})], \quad FL^e_{T,j} = T_e[q^{e^{II,j}}_{x_1}(x^e_{2,jp} - x^e_{2,j}) - q^{e^{II,j}}_{y}(x^e_{1,jp} - x^e_{1,j})], \tag{29}$$

where jp is the node of e following node j in counter-clock wise direction, $e^{II,j}$ represents the jth secondary element of e, $q^{e^{II,j}}_{x_1}$ and $q^{e^{II,j}}_{x_2}$ are the velocity components in the secondary element and C_e and T_e are the values of concentration and temperature of volume e. The volume concentration and heat fluxes are defined as

$$F^e_{C(T),j} = FL^e_{C(T),j} \quad \text{if} \quad FL^e_{C(T),j} > 0, F^e_{C(T),j} = -FL^{ep}_{C(T),m} \quad \text{if} \quad FL^e_{C(T),j} \leqslant 0, \tag{30}$$

where ep is the dual volume sharing side m with e.

After integration in space and time, applying the Green theorem to both convective and diffusive fluxes and discretizing the diffusive fluxes using a standard Galerkin formulation, prediction system (25) becomes:

$$\begin{aligned} \varepsilon \frac{C^{k+1/2}_e - C^k_e}{\Delta t}\sigma^e + \frac{1}{\Delta t}\sum_{j=1,Nlp}\int_{\Delta t} F^e_{C,j}dt &= -\int_\Omega \left(D^k_{ij}\frac{\partial w_n}{\partial x_i}\frac{\partial w_m}{\partial x_j}\right) C^k_m d\Omega, \\ (\varepsilon\rho c^l + (1-\varepsilon)\rho^s c^s)\frac{T^{k+1/2}_e - T^k_e}{\Delta t}\sigma^e + \rho c^l \frac{1}{\Delta t}\sum_{j=1,Nlp}\int_{\Delta t} F^e_{T,j}dt & \\ = -\int_\Omega \left(\Lambda^k_{ij}\frac{\partial w_n}{\partial x_i}\frac{\partial w_m}{\partial x_j}\right) T^k_m d\Omega, \;\; n,m = 1,\ldots,N, \;\; i,j = 1,2, & \end{aligned} \tag{31}$$

where σ^e is the area of cell e (the area of the polygon ABCDF in Fig. 2), Nlp is the number of sides of cell e, w is the shape function, equal to the weight function in the Galerkin formulation, Ω represents the 2D integration domain and N is the number of nodes in the domain. The integrals on the r.h.s. of system (31) represent the diffusive fluxes, function of the values of C and T as well as of the respective tensors $\mathbf{D}$ and $\mathbf{\Lambda}$ computed at the end of the previous time step.

If node e lies on the external boundary, the term of the convective fluxes $\frac{1}{\Delta t}\sum_{j=1,Nlp}\int_{\Delta t} F^e_{C(T),j}dt$ can be rewritten as $\frac{1}{\Delta t}\sum_{j=1,Nlp}\int_{\Delta t}\delta_j F^e_{C(T),j}dt + \frac{1}{\Delta t}\int_{\Delta t}(1-\delta_j)Q^{b,e}_{C(T)}dt$, where δ_j is equal to 1 or 0 if side j is, respectively an internal side of the polygon around node e, or not. $Q^{b,e}_{C(T)}$ is the pollutant (heat) supply or sink of cell e, depending on the flux sign and is assigned as Neumann condition if the flux enters the domain. The flux across side e–e_p is divided evenly between nodes e and e_p, as shown in Fig. 3 and the flux $Q^{b,e}_{C(T)}$ is given by the sum of the fluxes across the two external half-sides sharing node e (see Fig. 3).

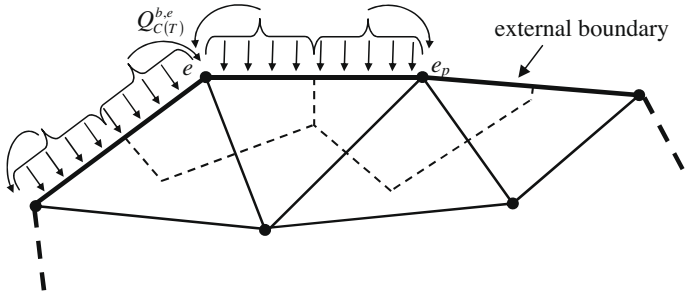

Fig. 3. External flux.

After the computation of the prediction components, the correction problem is solved assuming a second spatial approximation order (piecewise linear) for the unknown stream function, concentration and temperature. The diffusive correction system becomes (see Appendix 1):

$$\begin{aligned}
&\int_\Omega \left(\left(\frac{K_{ij}}{|\mathbf{K}|} \right)^{k+1/2} \frac{\partial w_n}{\partial x_i} \frac{\partial w_m}{\partial x_j} \right) \Psi_m d\Omega = 0 \quad i,j = 1,2, \\
&\varepsilon \frac{C_e^{k+1} - C_e^{k+1/2}}{\Delta t} \sigma^e + \int_\Omega \left(D_{ij}^{k+1/2} \frac{\partial w_n}{\partial x_i} \frac{\partial w_m}{\partial x_j} \right) C_m d\Omega = \int_\Omega \left(D_{ij}^{k} \frac{\partial w_n}{\partial x_i} \frac{\partial w_m}{\partial x_j} \right) C_m^k d\Omega, \\
&(\varepsilon \rho c^l + (1-\varepsilon)\rho^s c^s) \frac{T_e^{k+1} - T_e^{k+1/2}}{\Delta t} \sigma^e + \int_\Omega \left(\Lambda_{ij}^{k+1/2} \frac{\partial w_n}{\partial x_i} \frac{\partial w_m}{\partial x_j} \right) T_m d\Omega = \int_\Omega \left(\Lambda_{ij}^{k} \frac{\partial w_n}{\partial x_i} \frac{\partial w_m}{\partial x_j} \right) T_m^k d\Omega.
\end{aligned} \tag{32}$$

Observe that summing systems (31) and (32), the integral of the original system (20) is formally found again.

Because a scalar potential of the flow field exists, convective prediction system can be solved using a marching in space and time (MAST) procedure [2–4]. In this case it is always possible to order the cells in the computational domain according to their potential value and solve them sequentially, one after the other, from the highest to the lowest potential value. Because of the sign of the eigenvalues of the Jacobians $\mathbf{A}_1^{x_1}$ and $\mathbf{A}_1^{x_2}$, it is possible to solve each Eq. (25) if a polynomial approximation of the pollutant and heat volume convective fluxes entering from the upstream (in the potential scale) cells is always known.

Assume to know the pollutant and heat volume convective fluxes incoming from the boundary to any generic boundary cell e; these fluxes are given by polynomial time approximation, as will be further specified. According to this hypothesis, Eq. (31) can be solved as a system of two ordinary differential equations (ODEs) to be integrated in time from 0 to Δt. After the ODEs system in cell e is solved, the average leaving fluxes required for the solution of the downstream (in the potential scale) cells can be computed by partitioning the computed leaving flux through the sides of cell e shared with other downstream volumes.

The basic idea of the numerical technique is to compute the solution, within a given time step, by marching in space along the flux direction throughout the computational domain.

The three linear systems related to the three equations in system (32) are solved consecutively using a preconditioned conjugate gradient method; the systems are well-conditioned and the corresponding matrices are symmetric, positive-definite, with order equal to the number of the nodes in the domain. The first system is derived from the first equation in system (32), in the unknown Ψ. After the solution of the first system, the new spatial gradients of the stream function can be computed. The other two systems are derived from the second and the third equation of system (32), in the unknowns C and T, respectively, where the velocity components are computed according to the new spatial gradients of Ψ.

3.2.2. The case of variable-density groundwater transport problem

In the case of variable-density groundwater transport problem, a scalar potential of the flow field does not exist.

The original PDEs system (15) can be solved applying a fractional time step procedure similar to the one shown in the previous section. It is possible to extend the MAST procedure solving an additional convective correction step and using an auxiliary scalar function, called approximated potential, further defined.

The unknown vector $\mathbf{U}$ is

$$\mathbf{U} = (\ \Psi \quad C \quad T\ )^T. \tag{33}$$

Assume the flow velocity field to be function of the stream function gradients computed at the end of the previous time step:

$$q_{x_1} = -\frac{1}{\rho} \frac{\partial \Psi^k}{\partial x_2}, \quad q_{x_2} = \frac{1}{\rho} \frac{\partial \Psi^k}{\partial x_1}. \tag{34}$$

Assume also a scalar value ϕ_e^k, called approximated potential, to be known inside each cell at the beginning of each time step. After integration in time and according to Eq. (22a) we define the prediction step of system (15) as

$$\begin{aligned}
&\varepsilon \frac{C_e^{k+1/3} - C_e^k}{\Delta t} \sigma^e + \frac{1}{\Delta t} \left(1 - \frac{\bar{\alpha}}{C_s - C_0} \tilde{C} \frac{\rho_0}{\tilde{\rho}} \right) \sum_{j=1,Nlp} \int_{\Delta t} F_{C,j}^{p,e} dt + \frac{1}{\Delta t} \bar{\beta} \tilde{C} \frac{\rho_0}{\tilde{\rho}} \sum_{j=1,Nlp} \int_{\Delta t} F_{T,j}^{p,e} dt \\
&\quad = -\int_\Omega \left(D_{ij}^k \frac{\partial w_n}{\partial x_i} \frac{\partial w_m}{\partial x_j} \right) C_m^k d\Omega, \\
&\quad (\varepsilon \rho c^l + (1-\varepsilon)\rho^s c^s) \frac{T_e^{k+1/3} - T_e^k}{\Delta t} \sigma^e + \rho c^l \frac{1}{\Delta t} \left(1 + \bar{\beta} \tilde{T} \frac{\rho_0}{\tilde{\rho}} \right) \sum_{j=1,Nlp} \int_{\Delta t} F_{T,j}^{p,e} dt + \\
&\quad - \rho c^l \frac{1}{\Delta t} \frac{\bar{\alpha}}{C_s - C_0} \tilde{T} \frac{\rho_0}{\tilde{\rho}} \sum_{j=1,Nlp} \int_{\Delta t} F_{C,j}^{p,e} dt = -\int_\Omega \left(\Lambda_{ij}^k \frac{\partial w_n}{\partial x_i} \frac{\partial w_m}{\partial x_j} \right) T_m^k d\Omega \ n,m = 1,\ldots,N,
\end{aligned} \tag{35}$$

where

$$F_{C(T),j}^{p,e} = max(0, F_{C(T),j}^e) \quad \text{if} \quad \phi_e^k \geqslant \phi_{ep}^k \quad F_{C(T),j}^{p,e} = min(0, F_{C(T),j}^e) \quad \text{if} \quad \phi_e^k < \phi_{ep}^k. \tag{36}$$

The first correction system is defined as

$$\varepsilon\frac{C_e^{k+2/3}-C_e^{k+1/3}}{\Delta t}\sigma^e+\frac{1}{\Delta t}\left(1-\frac{\bar{\alpha}}{C_s-C_0}\widetilde{C}\frac{\rho_0}{\tilde{\rho}}\right)\sum_{j=1,Nlp}\int_{\Delta t}F_{C,j}^{c,e}dt+\frac{1}{\Delta t}\bar{\beta}\widetilde{C}\frac{\rho_0}{\tilde{\rho}}\sum_{j=1,Nlp}\int_{\Delta t}F_{T,j}^{c,e}dt=0$$

$$(\varepsilon\rho c^l+(1-\varepsilon)\rho^s c^s)\frac{T_e^{k+2/3}-T_e^{k+1/3}}{\Delta t}\sigma^e+\rho c^l\frac{1}{\Delta t}\left(1+\bar{\beta}\widetilde{T}\frac{\rho_0}{\tilde{\rho}}\right)\sum_{j=1,Nlp}\int_{\Delta t}F_{T,j}^{c,e}dt+$$

$$-\rho c^l\frac{1}{\Delta t}\frac{\bar{\alpha}}{C_s-C_0}\widetilde{T}\frac{\rho_0}{\tilde{\rho}}\sum_{j=1,Nlp}\int_{\Delta t}F_{C,j}^{c,e}dt=0, \tag{37}$$

where

$$F_{C(T),j}^{c,e}=max(0,F_{C(T),j}^{e})\quad\text{if}\quad\phi_e^k<\phi_{ep}^k\qquad F_{C(T),j}^{c,e}=min(0,F_{C(T),j}^{e})\quad\text{if}\quad\phi_e^k\geqslant\phi_{ep}^k, \tag{38}$$

in Eqs. (36) and (38) fluxes $F_{C(T),j}^{e}$ are defined as in Eqs. (29) and (30). If the convective pollutant and heat fluxes are leaving from cell e, terms $\widetilde{C}\widetilde{T}$ and $\tilde{\rho}$ are the concentration, temperature and liquid density of the cell; in the opposite case, $\widetilde{C}$, $\widetilde{T}$ and $\tilde{\rho}$ are the values of concentration, temperature and density of the neighbouring cells, numerically estimated from the single time values by means of Gaussian integration.

Observe that the source terms are neglected in system (37) since the irrotational components of the fluxes have been solved in the prediction problem. It can be easily shown that the first correction system has the same functional characteristics of the prediction system.

According to Eq. (22b), the second correction system becomes:

$$\int_\Omega\left(\left(\frac{K_{ij}}{|\mathbf{K}|}\frac{1}{\rho\mu_r}\right)^{k+2/3}\frac{\partial w_n}{\partial x_i}\frac{\partial w_m}{\partial x_j}\right)\Psi_m d\Omega=\int_\Omega\left(\frac{\partial w_n}{\partial x_1}\right)\rho_{r,m}^{k+2/3}d\Omega\quad i,j=1,2,$$

$$\varepsilon\frac{C_e^{k+1}-C_e^{k+2/3}}{\Delta t}\sigma^e+\int_\Omega\left(D_{ij}^{k+2/3}\frac{\partial w_n}{\partial x_i}\frac{\partial w_m}{\partial x_j}\right)C_m d\Omega=\int_\Omega\left(D_{ij}^{k}\frac{\partial w_n}{\partial x_i}\frac{\partial w_m}{\partial x_j}\right)C_m^k d\Omega$$

$$(\varepsilon\rho c^l+(1-\varepsilon)\rho^s c^s)\frac{T_e^{k+1}-T_e^{k+2/3}}{\Delta t}\sigma^e+\int_\Omega\left(\Lambda_{ij}^{k+2/3}\frac{\partial w_n}{\partial x_i}\frac{\partial w_m}{\partial x_j}\right)T_m d\Omega=\int_\Omega\left(\Lambda_{ij}^{k}\frac{\partial w_n}{\partial x_i}\frac{\partial w_m}{\partial x_j}\right)T_m^k d\Omega. \tag{39}$$

The system has been linearized assuming the tensors $\mathbf{D}$ and $\mathbf{\Lambda}$ on the l.h.s. of the second and third equations, as well as the term $\left(\frac{K_{ij}}{|\mathbf{K}|}\frac{1}{\rho\mu_r}\right)$ in the first equation, to be the same computed at the end of the first correction step.

We call the prediction system, the first and the second correction systems, respectively convective prediction (CP) system, convective correction (CC1) and diffusive correction (DC2) systems. Initial conditions of the CC1 system are the final values of the CP system and initial values of the DC2 system are the final values of the CC1 system. The values computed at the end of the CP step and at the end of the CC1 step are marked, respectively with index $k+1/3$ and $k+2/3$. The spatial gradients of the stream function Ψ for the computation of the velocity field is kept constant in time during both convective systems.

3.3. Solution of the CP and CC1 systems

Observe that, according to the flux definitions given in Eqs. (36) and (38), the flux integrals from cell e to cell ep in the CP step are only function of the cell e unknowns if $\phi_e^k\geqslant\phi_{ep}^k$ and are only function of the cell ep unknowns if $\phi_e^k<\phi_{ep}^k$. In the CC1 step the opposite holds. This allows to solve each system as a sequence of small ODEs systems, one for each computational cell, after ordering the cells according to their scalar potential. The priority is given to the cells with higher potential in the CP step and to the cells with lower potential in the CC1 step. Each ODEs system is integrated along the original time step using a Runge–Kutta method with adaptive step size control [40]. In the prediction step the ODEs system for the generic cell e is written as

$$\varepsilon\frac{dC_e}{dt}\sigma^e+\left(1-\frac{\bar{\alpha}}{C_s-C_0}\widetilde{C}\frac{\rho_0}{\tilde{\rho}}\right)\sum_{j=1,Nlp}F_{C,j}^{p,e}(t)+\bar{\beta}\widetilde{C}\frac{\rho_0}{\tilde{\rho}}\sum_{j=1,Nlp}F_{T,j}^{p,e}(t)=-\int_\Omega\left(D_{ij}^{k}\frac{\partial w_n}{\partial x_i}\frac{\partial w_m}{\partial x_j}\right)C_m^k d\Omega$$

$$(\varepsilon\rho c^l+(1-\varepsilon)\rho^s c^s)\frac{dT_e}{dt}\sigma^e+\rho c^l\left(1+\bar{\beta}\widetilde{T}\frac{\rho_0}{\tilde{\rho}}\right)\sum_{j=1,Nlp}F_{T,j}^{p,e}(t)-\rho c^l\frac{\bar{\alpha}}{C_s-C_0}\widetilde{T}\frac{\rho_0}{\tilde{\rho}}\sum_{j=1,Nlp}F_{C,j}^{p,e}(t)$$

$$=-\int_\Omega\left(\Lambda_{ij}^{k}\frac{\partial w_n}{\partial x_i}\frac{\partial w_m}{\partial x_j}\right)T_m^k d\Omega. \tag{40}$$

Call *out* the index of any side shared with any cell ep such that $\phi_e^k\geqslant\phi_{ep}^k$ in the CP step ($\phi_e^k<\phi_{ep}^k$ in the CC1 step). After the ODEs system of cell e is solved along the time step, the convective concentration and heat fluxes leaving through each side *out* have to be estimated in time.

If a 1st order time polynomial reconstruction (constant value in time) is chosen, the mean value of the leaving volume flux $\overline{F}_{C(T),out}^{p,e}$ through side *out* is estimated as

$$\overline{F}_{C,out}^{p,e}=\overline{C}_e[\bar{q}_{x_1}^{eII,out}(x_{2,outp}^e-x_{2,out}^e)-\bar{q}_{x_2}^{eII,out}(x_{1,outp}^e-x_{1,out}^e)],\quad\overline{F}_{T,out}^{p,e}=\overline{T}_e[\bar{q}_{x_1}^{eII,out}(x_{2,outp}^e-x_{2,out}^e)-\bar{q}_{x_2}^{eII,out}(x_{1,outp}^e-x_{1,out}^e)], \tag{41}$$

where the sub-index *outp* indicates the second node of side *out* in counter-clock wise direction and the over-score sign indicates the mean in time value: $\bar{q}_{x_1}^{e_{II,out}}$ and $\bar{q}_{x_2}^{e_{II,out}}$ are function of the spatial gradients of the stream function (constant in time) and of the mean in time value of the fluid phase density $\bar{\rho}^e$. This one has to be numerically estimated from the single time values. In the coded algorithm, density in seven Gauss points, selected in the time interval $0-\Delta t$, has been computed using a C^1 interpolation of the solution values produced by the Runge–Kutta method adopted for the solution of the ODEs system. $\overline{C}_e$ and $\overline{T}_e$ are the mean in time value of concentration and temperature in cell e, obtained by solving the following linear system given by the pollutant and heat mass balance equations:

$$\begin{aligned}
&\varepsilon\frac{C_e^{k+1/3}-C_e^k}{\Delta t}\sigma^e-\left(1-\frac{\bar{\alpha}}{C_s-C_0}\frac{\widetilde{\overline{C}}\rho_0}{\widetilde{\overline{\rho}}}\right)\sum_{j=1,Nlp}(1-\delta_{1j})\overline{F}_{C,j}^{p,e}-\bar{\beta}\widetilde{\overline{C}}\frac{\rho_0}{\widetilde{\overline{\rho}}}\sum_{j=1,Nlp}(1-\delta_{1j})\overline{F}_{T,j}^{p,e}\\
&+\int_\Omega\left(D_{ij}^k\frac{\partial w_n}{\partial x_i}\frac{\partial w_m}{\partial x_j}\right)C_m^k d\Omega=\left(1-\frac{\bar{\alpha}}{C_s-C_0}\frac{\widetilde{\overline{C}}\rho_0}{\widetilde{\overline{\rho}}}\right)\sum_{j=1,Nlp}\delta_{1j}\overline{F}_{C,j}^{p,e}+\bar{\beta}\widetilde{\overline{C}}\frac{\rho_0}{\widetilde{\overline{\rho}}}\sum_{j=1,Nlp}\delta_{1j}\overline{F}_{T,j}^{p,e},\\
&(\varepsilon\rho c^l+(1-\varepsilon)\rho^s c^s)\frac{T_e^{k+1/3}-T_e^k}{\Delta t}\sigma^e-\rho c^l\left(1+\bar{\beta}\widetilde{\overline{T}}\frac{\rho_0}{\widetilde{\overline{\rho}}}\right)\sum_{j=1,Nlp}(1-\delta_{1j})\overline{F}_{T,j}^{p,e}\\
&+\rho c^l\frac{\bar{\alpha}}{C_s-C_0}\frac{\widetilde{\overline{T}}\rho_0}{\widetilde{\overline{\rho}}}\sum_{j=1,Nlp}(1-\delta_{1j})\overline{F}_{C,j}^{p,e}+\int_\Omega\left(\Lambda_{ij}^k\frac{\partial w_n}{\partial x_i}\frac{\partial w_m}{\partial x_j}\right)T_m^k d\Omega\\
&=\rho c^l\left(1+\bar{\beta}\widetilde{\overline{T}}\frac{\rho_0}{\widetilde{\overline{\rho}}}\right)\sum_{j=1,Nlp}\delta_{1j}\overline{F}_{T,j}^{p,e}-\rho c^l\frac{\bar{\alpha}}{C_s-C_0}\frac{\widetilde{\overline{T}}\rho_0}{\widetilde{\overline{\rho}}}\sum_{j=1,Nlp}\delta_{1j}\overline{F}_{C,j}^{p,e},
\end{aligned}\tag{42}$$

where δ_{1j} is equal to is equal to 1 or 0 if the flux is, respectively leaving or entering the cell. $\widetilde{\overline{C}}$ and $\widetilde{\overline{T}}$ represent values of the concentration and temperature in the cell e numerically estimated from the single time values by means of Gaussian integration, similarly to $\bar{\rho}^e$. The summations on the l. h. s. of system (42) represent the mean in time values of the incoming pollutant and heat fluxes, known from the solution of the neighbour cells with higher potential. The summation on the r. h. s. represent the mean in time value of the fluxes leaving from sides *out* to lower potential cells, expressed as in Eq. (41).

A similar procedure is carried out for the solution of the CC1 system, written as

$$\begin{aligned}
&\varepsilon\frac{dC_e}{dt}\sigma^e+\left(1-\frac{\bar{\alpha}}{C_s-C_0}\widetilde{C}\frac{\rho_0}{\widetilde{\rho}}\right)\sum_{j=1,Nlp}F_{C,j}^{c,e}(t)+\bar{\beta}\widetilde{C}\frac{\rho_0}{\widetilde{\rho}}\sum_{j=1,Nlp}F_{T,j}^{c,e}(t)=0\\
&(\varepsilon\rho c^l+(1-\varepsilon)\rho^s c^s)\frac{dT_e}{dt}\sigma^e+\rho c^l\left(1+\bar{\beta}\widetilde{T}\frac{\rho_0}{\widetilde{\rho}}\right)\sum_{j=1,Nlp}F_{T,j}^{c,e}(t)-\frac{\bar{\alpha}}{C_s-C_0}\widetilde{T}\frac{\rho_0}{\widetilde{\rho}}\sum_{j=1,Nlp}F_{C,j}^{c,e}(t)=0.
\end{aligned}\tag{43}$$

The polynomial time reconstruction of the leaving fluxes is the same as in the prediction step, replacing in Eq. (42) the time levels k and $k+1/3$ respectively with $k+1/3$ and $k+2/3$.

3.4. The approximated scalar potential

Fractional step methodology provides accurate results only if the solution of the CP step is close to the final one of the current step; otherwise, the computation of the spatial gradients at different time levels can strongly affect the solution. In our case, to minimize the variables change in the CC1 step, it is important to choose an approximated potential with a gradient flux opposite in sign, as much as possible, to the water flux inside each computational element. If an exact potential exists and this condition is always attained, CC1 system vanishes in the following identities:

$$C^{k+2/3}=C^{k+1/3},\quad T^{k+2/3}=T^{k+1/3}.\tag{44}$$

Let's assign a value of the approximate potential function ϕ at each node and approximate the unknown potential function according to a Galerkin finite element approach by a trial function $\hat{\phi}$ given by

$$\hat{\phi}=\sum_{i=1,N}w^i\tilde{\phi}_i,\tag{45}$$

where w are the shape function related to the potential function and $\tilde{\phi}_i$ the unknown coefficients, further specified. We seek to minimize at the known time level t^k the following functional:

$$F=\sum_{e_T=1,Nel}(-\nabla\hat{\phi}-\mathbf{q})^2,\tag{46}$$

that is

$$F=\sum_{e_T=1,Nel}\left[\left(\sum_{m=1,N}-\frac{\partial w_m}{\partial x_1}\tilde{\phi}_m-q_{x_1}^{e_T}\right)^2+\left(\sum_{m=1,N}-\frac{\partial w_m}{\partial x_2}\tilde{\phi}_m-q_{x_2}^{e_T}\right)^2\right].\tag{47}$$

The proposed functional is convex and the minimum can be found by setting to zero the partial derivatives with respect to all the node approximated potentials

$$\frac{\partial F}{\partial \tilde{\phi}_m} = 0, m = 1, \ldots, N. \tag{48}$$

Eq. (48) can be written as

$$\frac{\partial F}{\partial \tilde{\phi}_m} = -\sum_{e_T=1,Nel}\left[\sum_{n=1,N}\left(-\frac{\partial w_m}{\partial x_1}\tilde{\phi}_n - q_{x_1}^{e_T}\right)\frac{\partial w_m}{\partial x_1}\right] - \sum_{e_T=1,Nel}\left[\sum_{n=1,N}\left(-\frac{\partial w_m}{\partial x_2}\tilde{\phi}_n - q_{x_2}^{e_T}\right)\frac{\partial w_m}{\partial x_2}\right] = 0. \tag{49}$$

Eq. (49) represents a linear system in the $\tilde{\phi}_n$ unknowns. The matrix of the system is sparse, symmetric, positive-definite and well-conditioned; the matrix elements are given by

$$A_{m,n} = \sum_{e_T}\left[\sum_{n}\frac{\partial w_m}{\partial x_1}\frac{\partial w_n}{\partial x_1} + \frac{\partial w_m}{\partial x_2}\frac{\partial w_n}{\partial x_2}\right], \tag{50}$$

and the mth source term of the system is

$$st_m = -\sum_{e_T}\left[\sum_{n}\frac{\partial w_m}{\partial x_1}q_{x_1}^{e_T} + \frac{\partial w_m}{\partial x_2}q_{x_2}^{e_T}\right], \tag{51}$$

where the velocity components are computed as

$$q_{x_1}^{e_T} = -\frac{1}{\bar{\rho}_{e_T}}\frac{\partial \Psi_{e_T}}{\partial x_2}, \quad q_{x_2}^{e_T} = \frac{1}{\bar{\rho}_{e_T}}\frac{\partial \Psi_{e_T}}{\partial x_1}. \tag{52}$$

$\bar{\rho}_{e_T}$ is the mean value of the fluid phase density of element e_T, given by a weighted mean of the density of its nodes. Spatial gradients of Ψ and $\bar{\rho}_{e_T}$ are computed at time level t^k and are kept constant during the time step.

3.5. Boundary conditions for the convective systems

Diffusive pollutant and heat fluxes (second terms on the r.h.s. of Eq. (40)) are assumed zero along both permeable and impermeable boundaries. To compute the convective fluxes along boundary sides we proceed as follows.

Case (1): Flux through the boundary side is entering the domain. Two possibilities exist. Case (1a): boundary liquid flux and concentration and/or temperature values are assigned; then the following equalities hold:

$$\begin{aligned} &F_{C(T),j}^{p,e} = BF_{C(T),j}^{e} \quad \text{with} \quad BF_{C,j}^{e} = C_{b,e}[q_{x_1,b,j}^{e}(x_{2,jp}^{e} - x_{2,j}^{e}) - q_{x_2,b,j}^{e}(x_{1,jp}^{e} - x_{1,j}^{e})] \quad \text{and} \\ &BF_{T,j}^{e} = T_{b,e}[q_{x_1,b,j}^{e}(x_{2,jp}^{e} - x_{2,j}^{e}) - q_{x_2,b,j}^{e}(x_{1,jp}^{e} - x_{1,j}^{e})], \end{aligned} \tag{53}$$

where $q_{x_1,b,j}^{e}$ and $q_{x_2,b,j}^{e}$ are the assigned boundary velocity components on side j of cell e and $C_{b,e}$ and $T_{b,e}$ are the assigned nodal concentration and temperature values (Dirichlet condition for C and T). Case (1b): only concentration and temperature boundary values are assigned. In this case Eq. (53) holds, but the boundary velocity components are computed as function of the spatial gradients of the stream function inside element e computed at the beginning of the time step.

Case (2): The flux through the boundary side is leaving the domain. In this case conditions (29) and (30) hold, where C and T are computed by solving the ODEs system in the cell with the boundary side and velocity components are computed according to the values of the density inside the cell and to the spatial gradients of the stream function at the beginning of the time step.

Case (3): impervious boundary side. The flux through an impervious side is zero and the following relationships hold:

$$F_{C(T),j}^{p,e} = 0. \tag{54}$$

We assume in cases (1)–(3) the scalar potential immediately outside the boundary sides consistent with the flux sign. This implies the convective concentration and heat fluxes to be zero in the CC1 step, that is

$$F_{C(T),j}^{c,e} = 0. \tag{55}$$

3.6. Solution of the DC systems

After the prediction component of C and T are found, a continuous piecewise linear shape is assigned to Ψ, C and T. Moving from the constant to the linear spatial approximation for C and T, would not change the global mass estimation at the given time level, if the polygons of the first approximation were delimited with the center of mass of the triangles. Since the axis centers are used, a small mass error is introduced. This error is balanced in the following by using the area σ^e of the same polygons as the coefficients of the diffusive correction components time derivatives in the FE formulation (see Appendix 1).

The sequential solution of three linear systems, each one associated to each of the Eq. (39), is required; the matrix of the corresponding systems is symmetric, positive-defined, with order equal to the number of the nodes in the domain.

The first system, in the Ψ unknown, can be written in compact form as

$$\mathbf{R}_{\Psi}\Psi = \mathbf{S}_{\Psi}, \tag{56}$$

where $\mathbf{R}_\Psi$ is the stiffness matrix and $\mathbf{S}_\Psi$ is the source term vector. Elements of $\mathbf{R}_\Psi$ and $\mathbf{S}_\Psi$ can be computed as the sum of the contributions given by the local stiffness matrix and the source term vector of each element in the domain. The $\mathbf{R}_\Psi$ and $\mathbf{S}_\Psi$ terms are:

$$R_{\Psi^{m,n}} = \sum_{e_T=1,Nel} R^{e_T}_{\Psi^{m,n}} = \sum_{e_T=1,Nel} \int_{\Omega^{e_T}} \left(\left(\frac{K^{e_T}_{ij}}{|\mathbf{K}^{e_T}|} \frac{1}{(\bar{\rho}\bar{\mu}_r)^{e_T}} \right)^{e_T,k+2/3} \frac{\partial w_n}{\partial x_i} \frac{\partial w_m}{\partial x_j} \right) d\Omega$$

$$S_{\Psi^m} = \sum_{e_T=1,Nel} S^{e_T}_{\Psi^m} = \sum_{e_T=1,Nel} \int_{\Omega^{e_T}} \left(\frac{\partial w_m}{\partial x_1} \right) \bar{\rho}^{e_T,k+2/3}_{r,m} d\Omega \quad i,j = 1,2; \quad m,n = 1,\ldots,N, \tag{57}$$

where the over-score bar indicates the mean values of ρ, ρ_r and μ_r inside the triangular element e_T, computed at the end of the convective steps.

After the solution of the first system, the new spatial gradients of the stream function are computed and used for the solution of the next two systems. These two systems have to be solved in the unknowns C and T and the velocity components inside each triangular element are computed according to the new spatial gradients of Ψ. The second system can be written in vector–matrix form as

$$\mathbf{R}_C \mathbf{C} + \mathbf{C}_C \frac{d\mathbf{C}}{dt} = \mathbf{S}_C, \tag{58}$$

where $\mathbf{R}_C$ and $\mathbf{C}_C$ are respectively the stiffness and the capacity matrices and $\mathbf{S}_C$ is the source term vector, given, similarly to the previous case, by the sum of the local matrices and source term vectors:

$$R_{C^{m,n}} = \sum_{e_T=1,Nel} R^{e_T}_{C^{m,n}} = \sum_{e_T=1,Nel} \int_{\Omega^{e_T}} \left(D^{e_T,k+2/3}_{ij} \frac{\partial w_n}{\partial x_i} \frac{\partial w_m}{\partial x_j} \right) d\Omega$$

$$C_{C^{m,n}} = \sum_{e_T=1,Nel} C^{e_T}_{C^{m,n}} = \sum_{e_T=1,Nel} \int_{\Omega^{e_T}} w_n w_m \frac{\bar{\varepsilon}^{e_T}}{\Delta t} d\Omega$$

$$S_{C^m} = \sum_{e_T=1,Nel} S^{e_T}_{C^m} = \sum_{e_T=1,Nel} \int_{\Omega^{e_T}} \left(D^{e_T,k}_{ij} \frac{\partial w_n}{\partial x_i} \frac{\partial w_m}{\partial x_j} \right) d\Omega, \tag{59}$$

where the over-score sign has the same meaning before specified.

Similarly, the third system in the unknowns T can be written as

$$\mathbf{R}_T \mathbf{T} + \mathbf{C}_T \frac{d\mathbf{T}}{dt} = \mathbf{S}_T, \tag{60}$$

where the elements of the stiffness matrix $\mathbf{R}_T$, of the capacity matrix $\mathbf{C}_T$, as well as of the source term vector $\mathbf{S}_T$, are given by

$$R_{T^{m,n}} = \sum_{e_T=1,Nel} R^{e_T}_{T^{m,n}} = \sum_{e_T=1,Nel} \int_{\Omega^{e_T}} \left(\Lambda^{e_T,k+2/3}_{ij} \frac{\partial w_n}{\partial x_i} \frac{\partial w_m}{\partial x_j} \right) d\Omega$$

$$C_{T^{m,n}} = \sum_{e_T=1,Nel} C^{e_T}_{T^{m,n}} = \sum_{e_T=1,Nel} \int_{\Omega^{e_T}} w_n w_m \frac{(\bar{\varepsilon}\rho c^l + (1-\bar{\varepsilon})\rho^s c^s)^{e_T}}{\Delta t} d\Omega$$

$$S_{T^m} = \sum_{e_T=1,Nel} S^{e_T}_{T^m} = \sum_{e_T=1,Nel} \int_{\Omega^{e_T}} \left(\Lambda^{e_T,k}_{ij} \frac{\partial w_n}{\partial x_i} \frac{\partial w_m}{\partial x_j} \right) d\Omega. \tag{61}$$

$K^{e_T}_{ij}, D^{e_T}_{ij}, \Lambda^{e_T}_{ij}$ in Eqs. (57), (59) and (61) are the tensors of the hydraulic conductivity, hydrodynamic dispersion and hydrodynamic–thermo-dispersion of e_T, assumed constant inside the triangular element.

A fully implicit time discretization has been chosen for the solution of the systems (56), (58) and (60), that is:

$$\mathbf{R}_\Psi \Psi^{k+1} = \mathbf{S}_\Psi, \tag{62a}$$

$$\mathbf{R}_C \mathbf{C}^{k+1} + \mathbf{C}_C \frac{\mathbf{C}^{k+1} - \mathbf{C}^{k+2/3}}{\Delta t} = \mathbf{S}_C, \tag{62b}$$

$$\mathbf{R}_T \mathbf{T}^{k+1} + \mathbf{C}_T \frac{\mathbf{T}^{k+1} - \mathbf{T}^{k+2/3}}{\Delta t} = \mathbf{S}_T. \tag{62c}$$

This guarantees unconditional stability with regard to the time step size. The time discretization provides a diffusive effect that goes to zero along with the time step size.

3.7. Boundary conditions for the DC systems

3.7.1. Boundary conditions for the stream function

According to the relationships between the stream function and the flow velocity (see Eq. (5)), it can be easily shown that the appropriate boundary condition for the stream function along the Γ_1 part of the boundary, where the second type (Neumann) boundary condition holds for mass fluxes is

$$\Psi(x_1, x_2, t) = \Psi_1(x_1, x_2, t) \text{ on} \Gamma_1, \tag{63}$$

where Ψ_1 is the Dirichlet value of the stream function assigned on Γ_1, equal to:

$$\Psi(\Gamma) = \Psi_0(\Gamma_0) + \int_{\Gamma_0}^{\Gamma} \rho q_0 \cdot \mathbf{n} d\Gamma, \tag{64}$$

where $\mathbf{n}$ is a unit vector normal to the boundary Γ. Along the impervious boundaries Ψ is constant. Diffusive flux is computed a posteriori by means of Eqs. (62a) and (57).

It can be also shown [49] that the appropriate boundary condition for the stream function along the Γ_2 portion of the boundary where the first type (Dirichlet) boundary condition holds for the equivalent freshwater head (or pressure p) (Eq. (3)) is given by the following second type condition (see Fig. 4).

$$\frac{\partial \Psi}{\partial n} = \rho \hat{q} \cdot n_\Gamma, \tag{65}$$

where n_Γ is a unit vector parallel to the boundary Γ_2 and $\rho \hat{q} \cdot n_\Gamma$ is the mass flux component parallel to the boundary side (see Fig. 5). Eq. (65) can be written as [49]:

$$\frac{\partial \Psi}{\partial n} = -K_\Gamma \left(\frac{\partial h}{\partial \Gamma} + \rho_r \frac{\partial x_2}{\partial \Gamma} \right) \rho \mu_r, \tag{66}$$

where the sub-index Γ indicates properties on the boundary; integrating Eq. (66) over nodal segments of the domain, one gets:

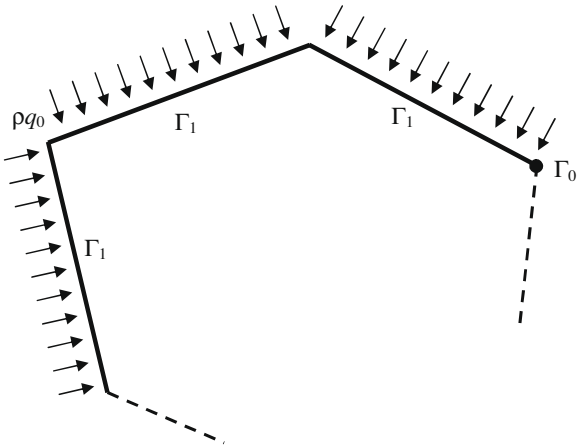

Fig. 4. Dirichlet boundary conditions for the stream function.

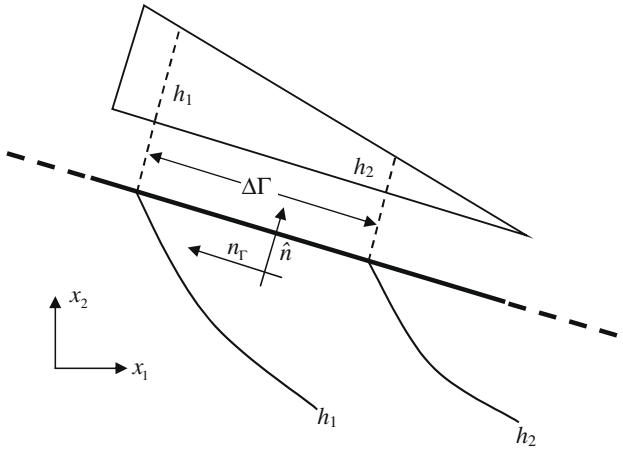

Fig. 5. Neumann boundary condition for the stream function.

$$\frac{\partial \Psi}{\partial n}\Delta\Gamma = -K_\Gamma(\Delta h + \rho_r \Delta x_2)\rho\mu_r, \tag{67a}$$

or

$$\frac{1}{\rho\mu_r}\frac{1}{K_\Gamma}\frac{\partial \Psi}{\partial n}\Delta\Gamma + \rho_r \Delta x_2 = -\Delta h, \tag{67b}$$

where $\Delta\Gamma$ is the length of the nodal segment of Γ and Δh and Δx_2 are measured along the segment. Along the horizontal boundaries the relative density term in Eq. (67b) vanishes.

3.7.2. Boundary conditions for concentration and temperature

The first type (Dirichlet) boundary condition is given by

$$C = C_1 \quad \text{on} \quad \Gamma_1, \quad T = T_1 \quad \text{on} \quad \Gamma_1, \tag{68}$$

where C_1 and T_1 are assigned values of C and T on the selected portion of the boundary Γ_1. The diffusive fluxes are computed a posteriori by means of Eqs. (62b) and (59), and Eqs. (62c) and (61).

Second type (Neumann) boundary condition: diffusive pollutant and heat fluxes are assumed zero along both permeable and impermeable boundaries, as previously explained for the boundary conditions of the convective steps.

4. Numerical tests

Benchmark analytical solutions for model validation are not available due to the non-linear nature of the variable-density flow and transport problem. Therefore a cross-validation of the results obtained by different numerical codes is carried out to test the proposed scheme.

We present results for four benchmark tests:

(1) The Henry test [29], a classic seawater intrusion problem.
(2) The Henry–Hilleke test [30], to investigate the effects of temperature-dependent density on coastal groundwater flow.
(3) The Elder test [20,21], a free convection problem (fingering problem), presented with and without thermohaline effects.
(4) The salt-dome test (HYDROCOIN level 1, case 5), presented with and without thermohaline effects.

Two grid-related dimensionless numbers that affect the accuracy of the proposed numerical scheme are the Courant number CFL and the Peclet number *Pe*. The first one is defined as

$$CFL = \frac{\Delta t|\mathbf{q}|}{\sqrt{\sigma^e}}. \tag{69}$$

The second one indicates the ratio between the advective and the diffusive term and is defined as (see for example [37]):

$$Pe = CFL\frac{\sigma^e}{\Delta t\|\mathbf{D}\|}, \tag{70}$$

where $\|\mathbf{D}\|$ is the norm of the tensor $\mathbf{D}$.

Since a fully implicit time discretization is used for the solution of the DC step, which guarantees unconditional stability with regard to Δt, CFL is related to the convective steps and both CFL and *Pe* numbers have been computed using the area σ^e of the dual volume and a fluid velocity function of the spatial gradients of Ψ computed at the end of the previous time step.

4.1. The Henry test [29]

In the Henry test the intrusion of a saltwater front inside a confined aquifer initially saturated with uncontaminated freshwater is computed. It has become a classic benchmark for variable-density flow models because of the existence of a semi-analytic steady-state solution derived by Henry [29]. In deriving his solution, the author assumed the so called Boussinesq approximation, which neglects the density variation within the mass balance equation of the fluid phase. Density variation is included in the buoyancy term of the Darcy equations only (the second term on the r.h.s. of Eq. (4)). Henry [29] obtained analytical expressions for the stream function and concentration in the form of Fourier series. Many authors [1,14,15,17,23,26,33,35,36,46,48,52,53] tested their numerical models with the Henry test. However, no numerical model has been able to properly reproduce the semi-analytical solution computed by Henry. This may be due also to some of the approximations adopted by Henry in his original findings, for example, starting from Eq. (1), the Boussinesq approximation requires perpendicular Darcy velocity vectors and density gradients.

Several numerical models based on different methods give similar results for the Henry test. These include a particle tracking model by Pinder and Cooper [46], a mixed Eulerian–Lagrangian scheme proposed by Galeati et al. [26], finite elements methods [23,33,48], the finite element model by the US Geological Survey, SUTRA [52,53], the finite elements codes

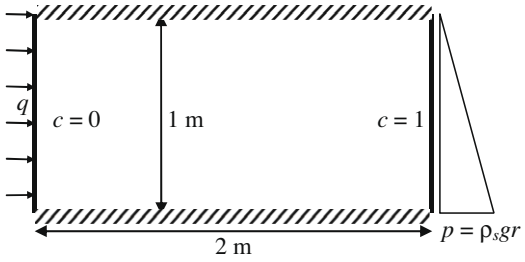

Fig. 6. Henry test: spatial domain and boundary conditions.

FEFLOW [14,15,17] and ROCKFLOW [35,36] and the combined mixed hybrid finite element and discontinuous finite element by Ackerer et al. [1].

The spatial domain of the aquifer and the boundary conditions are schematized in Fig. 6 (where $c = C/C_{max}$ is the relative concentration). Boundary conditions for flow are: impermeable top and bottom sides and a constant entering flux at the inland vertical side. Hydrostatic pressure is assumed along the vertical boundary of the sea side. At the inland side the concentration is zero which corresponds to freshwater. At the coastal side concentration of seawater is set, $c = 1$. Simulation parameters of the test are reported in Table 1.

The relationship between the viscosity μ and the concentration is [17]:

$$\mu = \mu_0(1 + 1.85\omega - 4.1\omega^2 + 44.1\omega^3), \omega = 10^{-6}C. \tag{71}$$

Spatial domain has been discretized with 1600 rectangular isosceles triangular elements (see Fig. 7(a)) and the time step size is 20 s; the value of the molecular diffusion coefficient D_d is 18.86×10^{-6} m^2 s^{-1}. The isopleths 0.25, 0.5 and 0.75 of the maximum concentration, the stream function contours and the velocity field obtained by MAST FV/FE are shown in Figs. 8(a)–8(c) after 120 min, a time long enough to reach steady-state condition. The maximum CFL value is 1.0536 and the maximum Peclet number is approximately 6.65. In Fig. 8(a) the revised analytical solution proposed by Segol [47] is shown too for the isopleths 0.25 and 0.5. MAST FV/FE results are in good agreement with the analytical solution. Using a different mesh, with

Table 1
Henry test – parameters values.

Parameter	Symbol	Units	Value
Molecular diffusion coefficient	D_d	(m^2/s)	6.6 or 18.86×10^{-6}
Longitudinal solute dispersivity	β_L	(m)	0
Transversal solute dispersivity	β_T	(m)	0
Permeability tensor	k	(m^2)	1.019368×10^{-9}
Density ratio	$\bar{\alpha}/C_s$	(–)	0.025
Porosity	ε	(–)	0.35
Reference fluid density	ρ_0	(kg/m^3)	1000
Maximum density of the solution	ρ_s	(kg/m^3)	1025
Reference fluid viscosity	μ_0	(kg/m/s)	0.001
Flux at the inland boundary	q	(m/s)	8.333×10^{-5}

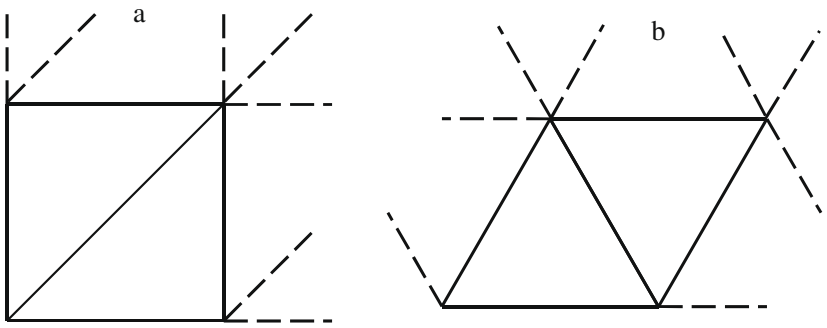

Fig. 7. Computational mesh.

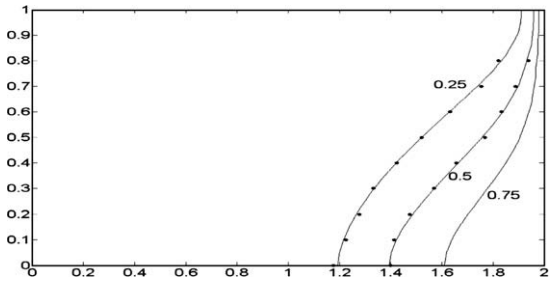

Fig. 8(a). Henry test: MAST FV/FE computed isopleths (solid lines) versus analytical solution by Segol [47] (circular dots) (*Nel* 1600).

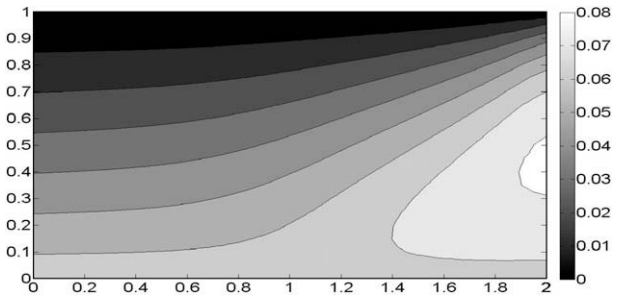

Fig. 8(b). Henry test: MAST FV/FE computed stream function profiles (*Nel* 1600).

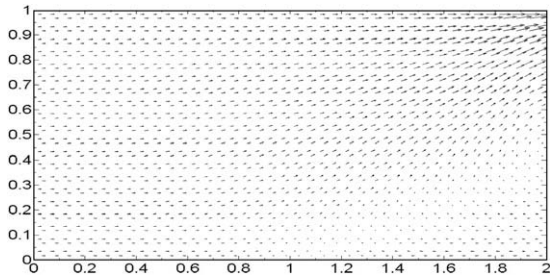

Fig. 8(c). Henry test: MAST FV/FE computed velocity field (*Nel* 1600).

the hypotenuse of the triangular elements orthogonal to the hypotenuses of the previous mesh, very close results are obtained, not shown for brevity.

In Fig. 9 the numerical results computed by MAST FV/FE scheme are compared with the numerical solution by Ackerer et al. [1] for the same value of D_d. The authors applied a MHFE scheme to solve the flow equation and the diffusive part of the transport equation and a discontinuous finite element method for the convective part of the transport equation. Acker-

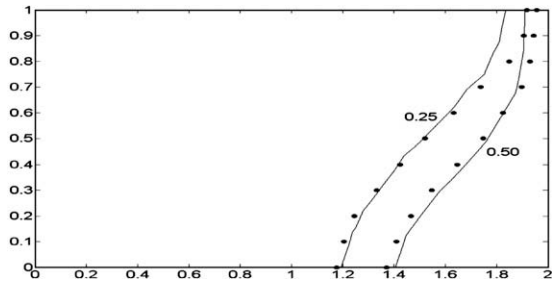

Fig. 9. Henry test: MAST FV/FE computed isopleths (solid lines) versus numerical solution by Ackerer et al. [1] (circular dots) (*Nel* 256).

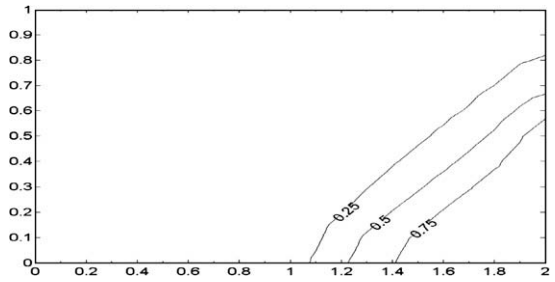

Fig. 10(a). Henry test: MAST FV/FE computed isopleths (*Nel* 400, modified boundary conditions for concentration).

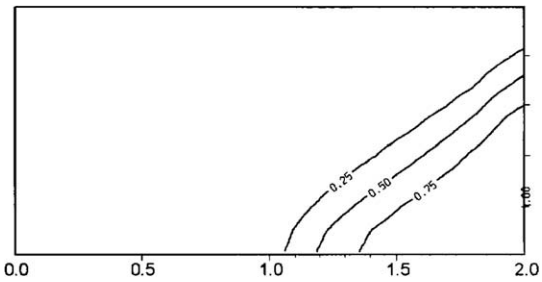

Fig. 10(b). Henry test: FEFLOW computed isopleths [17] (modified boundary conditions for concentration).

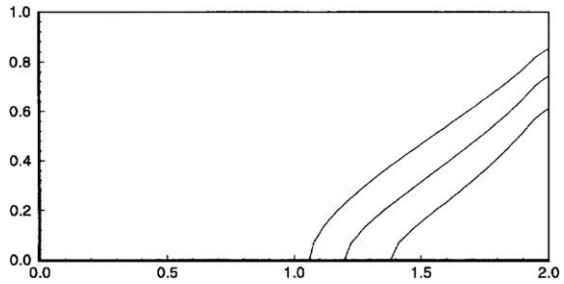

Fig. 10(c). Henry test: ROCKFLOW computed isopleths (modified boundary conditions for concentration).

er et al. [1] discretized the spatial domain with 20 × 10 quadrilateral elements. Results of the MAST FV/FE scheme have been obtained using a mesh with 256 rectangular isosceles triangular elements with area 0.007813 m^2 and a $\Delta t = 50$ s. The maximum CFL value is 0.77. Comparing MAST FV/FE results in Figs. 8(a) and 9, main differences occur near the upper right-hand corner, characterized by the highest velocities. In this part of the domain the velocity solution of Ackerer et al. [1] is likely to be more accurate because of the higher solution order of the method and of the velocity continuity along the triangular element sides.

Many authors modified the Henry test with a mixed seawater and freshwater boundary on the left hand side, assuming seawater concentration from $x_2 = 0$ to $x_2 = 0.5$ m [23]. In Figs. 10(a)–10(c) MAST FV/FE results at steady-state are compared with the corresponding ones provided by FEFLOW [15,17] and ROCKFLOW [35,36] for $D_d = 6.6 \times 10^{-6}$ m^2 s^{-1} [34]. A mesh with 400 triangular isosceles elements and a $\Delta t = 50$ s has been used in the MAST FV/FE simulations, run with a maximum CFL number equal to 1.04. FEFLOW and ROCKFLOW simulators are based on the Galerkin FE method and solve the balance equations written in terms of hydraulic head and mass concentration (FEFLOW) and pressure and mass fraction of pollutant (ROCKFLOW). The spatial domain is discretized with 200 quadrilateral elements, in FEFLOW simulations and with 581 triangular elements in ROCKFLOW simulations. MAST FV/FE results are in good agreement with the ones provided by both literature models.

4.2. The Henry–Hilleke test [30]

In 1972 Henry and Hilleke investigated the effects of temperature-dependent density on coastal groundwater flow. The test simulates seawater intrusion in a confined aquifer where freshwater recharge flows from an inland boundary over more

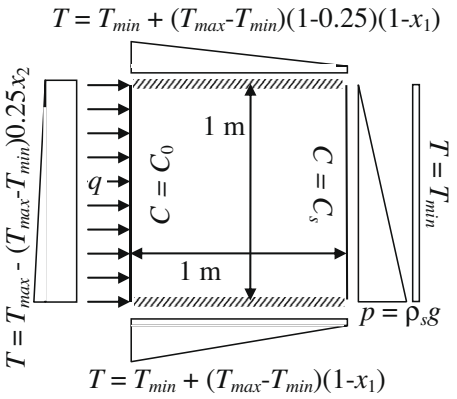

Fig. 11. Henry–Hilleke test: spatial domain and boundary conditions.

Table 2
Henry–Hilleke test – parameters values.

Parameter	Symbol	Units	Value
Maximum concentration of the solution	C_s	(kg/m^3)	35.7
Reference concentration	C_0	(kg/m^3)	0
Maximum temperature	T_{max}	(°C)	50
Minimum temperature	T_{min}	(°C)	5
Thermal capacity of fluid	ρc^l	(J/m^3/°C)	4.182×10^6
Thermal capacity of solid	$\rho^s c^s$	(J/m^3/°C)	0
Molecular diffusion coefficient	D_d	(m^2/s)	2.381×10^{-6}
Longitudinal solute dispersivity	β_L	(m)	0
Transversal solute dispersivity	β_T	(m)	0
Permeability tensor	k	(m^2)	1.019×10^{-9}
Density ratio	$\bar{\alpha}/C_s$	(–)	0.7×10^{-3}
Thermal expansion coefficient	$\bar{\beta}$	(°C^{-1})	0.375×10^{-3}
Porosity	ε	(–)	0.35
Thermal conductivity of fluid	λ^l	(J/m/s/°C)	9.952×10^2
Thermal conductivity of solid	λ^s	(J/m/s/°C)	0
Longitudinal solute thermodispersivity	α_L	(m)	0
Transversal solute thermodispersivity	α_T	(m)	0
Reference fluid density	ρ_0	(kg/m^3)	1000
Maximum density of the solution	ρ_s	(kg/m^3)	1200
Reference fluid viscosity	μ_0	(kg/m/s)	0.001
Flux at the inland boundary	q	(m/s)	8.333×10^{-5}

saline water derived from a seawater boundary. Spatial domain and boundary conditions for concentration and temperature are shown in Fig. 11. Initially aquifer has hydrostatic pressure, with freshwater concentration ($C = 0$ kg/cm) and isothermal conditions ($T = T_0 = T_{min} = 5$ °C). At $t = 0$ heat begins to be transported inward from the top, bottom and left boundaries and seawater begins to intrude the freshwater by moving laterally from the right boundary. Temperature gradients at the top, bottom and freshwater sides increase vertical freshwater movement and intrusion of seawater at the base of the aquifer when compared to a similar isothermal case. The coefficients used in the test are reported in Table 2. The dependence of the viscosity μ on concentration and temperature has been neglected.

In Figs. 12(a)–12(b) results by MAST FV/FE are compared with the corresponding ones computed with SUTRA-MS (saturated–unsaturated transport of multiple species) [32] and SEAWAT [50] schemes. In both the numerical procedures the unknown variables are the fluid pressure, the concentration and the temperature. SUTRA-MS [32] is a modified version of SUTRA model [52,53], capable of simulating variable-density flow, as well as transport of heat and multiple dissolved species through variably saturated porous media. SUTRA uses a hybridized Galerkin FE method and implicit finite-difference technique to solve the fluid mass balance equation and unified energy- and solute-balance equation for variable-density, single-phase, saturated–unsaturated flow and single-species transport. SUTRA uses bilinear quadrilateral elements in 2D. SEAWAT [27,28] is a finite-difference code designed to simulate coupled variable-density and transport solute in groundwater flow. In 2006, Thorne et al. [50] proposed a new version of the code that adds the ability to simultaneously model energy and solute transport.

In MAST FV/FE numerical simulations a mesh with 1250 rectangular isosceles triangular elements and $\Delta t = 60$ s have been used (solid black lines in Fig. 12); the maximum CFL value is 1.54.

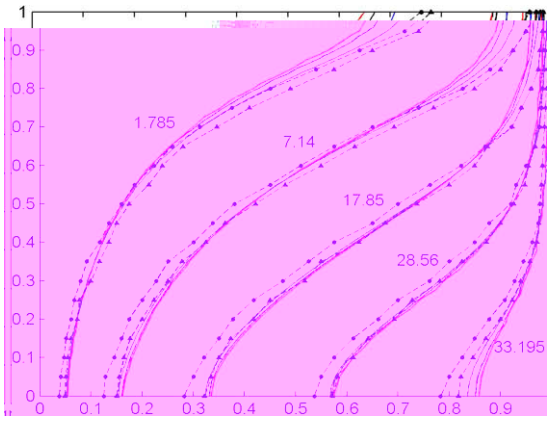

Fig. 12(a). Henry–Hilleke test: MAST FV/FE computed isopleths (solid lines) versus SEAWAT [50] results (dashed lines with circular dots) and SUTRA-MS [32] results (dashed lines with triangular dots).

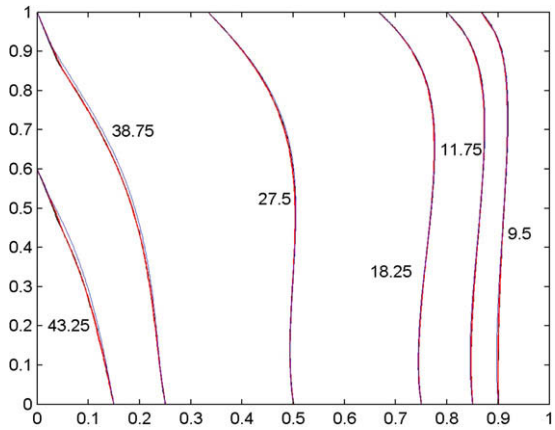

Fig. 12(b). Henry–Hilleke test: MAST FV/FE computed temperatures.

In both SEAWAT and SUTRA-MS simulations a mesh of 40 by 40 quadrilateral elements has been used, with the same Δt. Simulations are stopped after 3.3 h, sufficient for the simulation to reach steady-state conditions.

MAST FV/FE results are in quite good agreement with the ones provided by both models. In Fig. 12(b), temperature profiles of both literature models are not distinguishable from the ones provided by MAST FV/FE at the graphic scale.

The effects of the mesh size on the numerical results have been also investigated. In Fig. 12 results computed by MAST FV/FE using the same Δt and meshes with 3200 and 800 elements (blue and red lines respectively) are compared with the previous ones obtained with 1250 elements; the maximum CFL values are 3.166 and 1.01, respectively. The effects of the mesh size are generally negligible, more evident for the smallest concentration values and in the parts of the domain characterized by the highest flow velocities. In Figs. 13(a)–13(c) the stream function profiles and the velocity field are shown.

4.3. The Elder test [20,21]

Elder [20,21] presented experimental and numerical studies concerning the thermal convection produced by heating the inferior surface of a porous layer. The flow inside the box was prompted by a vertical temperature gradient. Thermally induced density gradient caused a complex pattern of the denser water throughout the box; for the characteristics of these patterns, this test is also denoted as fingering problem. This problem was studied both physically, in laboratory with the use of Hele-Shaw cells, as well as numerically. Elder [21] developed a modified problem with parameters suited to porous media flow where the density dependence was due by solute variations. This modified test became one of the most used benchmark problem used for testing density-dependent groundwater codes and it is referred as Elder salt convection problem.

In the following of the paper we will investigate both the salt convection problem as well as its thermohaline extension.

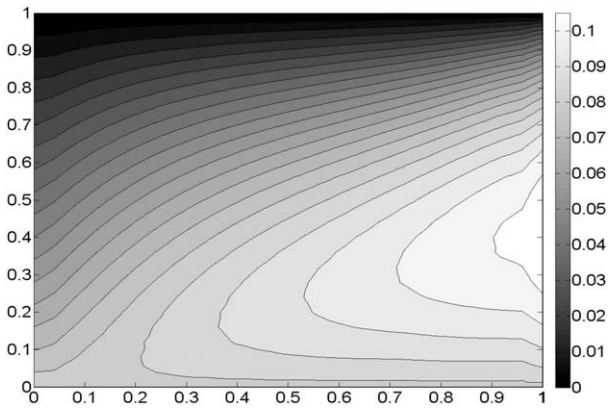

Fig. 13(a). Henry–Hilleke test: MAST FV/FE computed stream function profiles.

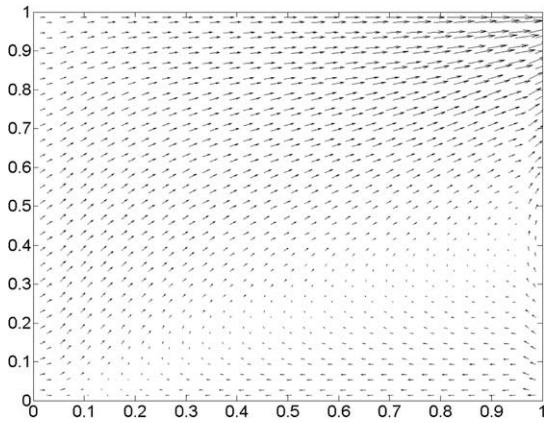

Fig. 13(b). Henry–Hilleke test: MAST FV/FE computed velocity field.

4.3.1. The Elder salt convection problem

The spatial domain, the initial and the boundary conditions are shown in Fig. 14. The computational domain is a closed rectangular box with a source of solute located in the central part of the upper boundary. On this part of the boundary a salt solid surface provides a specified concentration with value $c = 1$. On all the lower boundary an adsorbing surface guarantees the concentration $c = 0$. A zero value of the fluid pressure is assumed at each upper corner; hydrostatic pressure distribution and zero concentration are assumed initially inside the domain. Fluid flow is driven by fluid density difference. The parameters for this problem are given in Table 3. The problem involves total density variation of 20% which makes this a strongly coupled flow case. The relationship between μ and C is expressed by Eq. (71). The problem is symmetrical at $x = 300$ m so it is important to investigate the symmetry of the numerical results.

For the numerical simulations a mesh with 1414 equilateral triangular elements (see Fig. 7(b)) with side 12 m and 772 nodes has been used, with $\Delta t = 1$ month. The maximum CFL number value is 0.94. In Fig. 15 the computed isopleths are

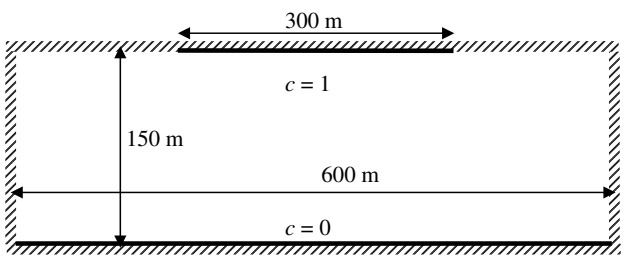

Fig. 14. Elder test: spatial domain and boundary conditions.

Table 3
Elder test – parameters values.

Parameter	Symbol	Units	Value
Molecular diffusion coefficient	D_d	(m^2/s)	3.566×10^{-6}
Longitudinal solute dispersivity	β_L	(m)	0
Transversal solute dispersivity	β_T	(m)	0
Permeability tensor	k	(m^2)	4.845×10^{-13}
Density ratio	$\bar{\alpha}/C_s$	(–)	0.2
Porosity	ε	(–)	0.1
Reference fluid density	ρ_0	(kg/m^3)	1000
Maximum density of the solution	ρ_s	(kg/m^3)	1200
Reference fluid viscosity	μ_0	(kg/m/s)	0.001

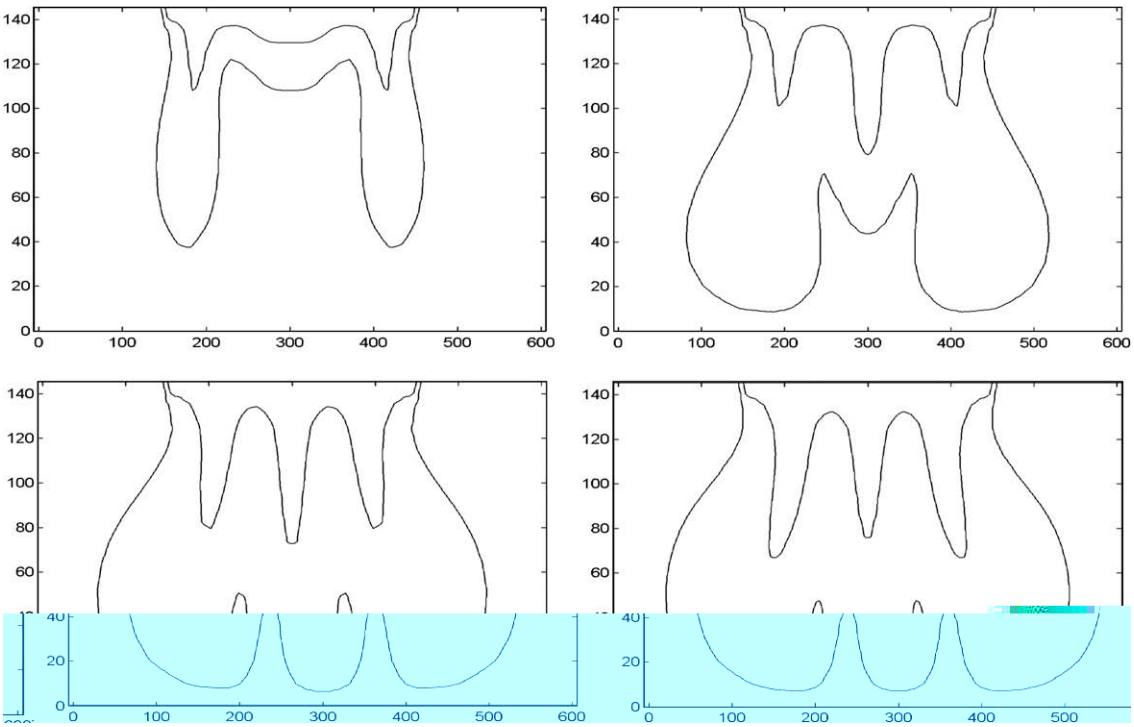

Fig. 15. Elder test: MAST FV/FE computed isopleths (4, 10, 15 and 20 years).

shown for 20% and 60% of the maximum concentration at the simulation times $T = 4$, 10, 15 and 20 years. In Fig. 16 the numerical results by FEFLOW [34], obtained using a mesh with 1100 quadrilateral elements and 1170 nodes, are shown too for the same simulation times. The differences between MAST FV/FE and FEFLOW results are significant. These could depend on the physical "instability" of the Elder problem, that amplifies the effect of the numerical discretization on the final results. Anyway, the downwelling direction of the central flux is the same in both numerical models.

When dealing with such kind of problem, characterized by formation of fingers, two fundamental questions arise, namely: the role of the grid size on the accuracy of the numerical solution and the relationship between the number of captured fingers and the mesh density. A quite coarse mesh with 357 triangular equilateral elements (length side is 24 m) and 212 nodes (level mesh 0th) has been generated and used as the basis for further refinements. At each refinement level $i + 1$, each triangle of the previous ith mesh is subdivided in four equal triangles (see Fig. 17). The 0th level mesh has a Δt equal to 2 months; for the next level meshes time step size has been halved, in order to limit the growth of the maximum CFL number, that ranges from 0.88 to 2.034 from the coarsest to the finest mesh. Peclet number ranges between 4.3 and 5.6. In Figs. 18–21 the computed isopleths are shown for 20 and 60% of the maximum concentration for the five mesh levels and for the simulation times $T = 4$, 10, and 20 years (results for the 1st level mesh are the ones shown in Fig. 15).

At early simulation time (4 years) the number of captured fingers vary, increasing with the mesh density from level 0th to level 2nd; solutions obtained for levels 3rd and 4th are very close to the one for level 2nd. In the numerical results fingers develop because of the numerical perturbations due to the spatial and temporal discretization. Small perturbations appear in the numerical solutions at discrete mesh points, causing the inception of fingers. Consequentially, increasing the number of

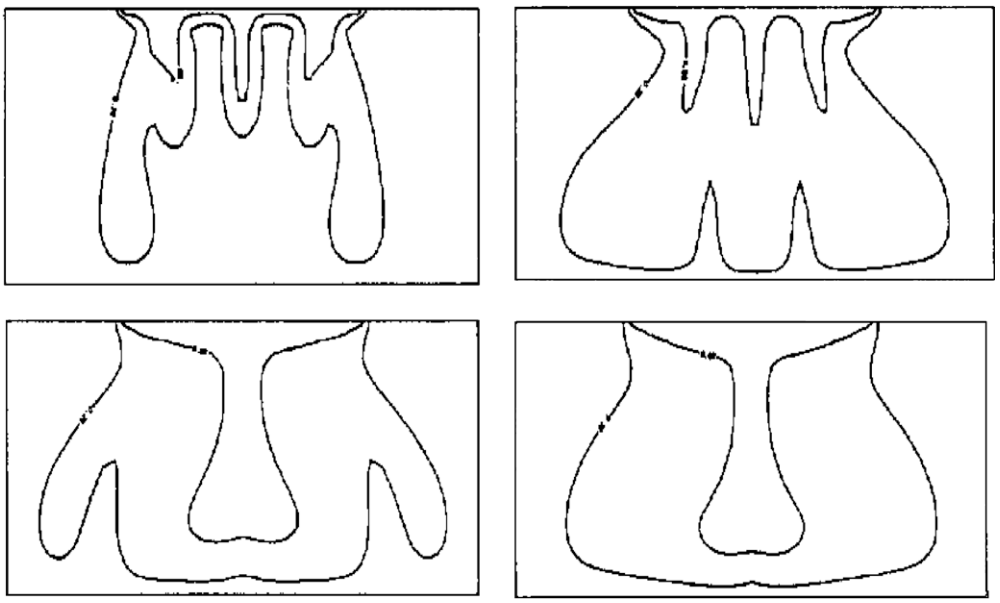

Fig. 16. Elder test: FEFLOW [34] computed isopleths (4, 10, 15 and 20 years).

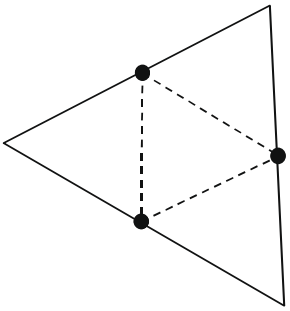

Fig. 17. Mesh refinement.

mesh points, the number of captured fingers increases. At higher simulation times, except for the coarsest mesh level (0th), the number of the fingers is the same because of the effect of the dispersion phenomena, responsible for the coalescence of smaller fingers into larger ones.

Observe also that at the simulation time 20 years, for the coarsest level mesh (namely level 0th), the flow upwells in the middle section of the domain; refining the mesh (levels 1st, 2nd, 3rd and 4th), a downwelling flow appears. The inversion of the central flow due to the mesh refinement has been observed by other authors in literature, as summarized in Table 4. Observe that refining the computational mesh size, the central flow direction remains the same in MAST FV/FE results, while its changes in other literature numerical model tests.

4.3.2. The Elder thermohaline problem

The salt convective Elder problem is expanded to a thermohaline convection process if the salinity field is coupled with a thermal distribution. The aquifer is permanently heated from below and the salinity gradient acts from above. The normalized concentration on the top side of the domain is equal to the maximum value in the central part and the salinity is held at zero on the bottom side. The top and bottom boundaries are held at constant temperature as shown in Fig. 22. All remaining boundaries are assumed impervious for solute and adiabatic for heat. All the boundaries are impervious for the fluid flow. Model parameters are listed in Table 5. The relationship between μ and C and T is given by [17]:

$$\mu = \mu_0 \frac{(1 + 1.85\omega - 4.1\omega^2 + 44.1\omega^3)}{(1 + 0.7063\varsigma - 0.048\varsigma^3)} \omega = 10^{-6} C \; \varsigma = \frac{T - 150}{150}. \tag{72}$$

The thermohaline Elder problem can be considered as a mixed double diffusive convection process, where a finger regime dominates at the beginning (cool salinity sinks down) and later a more diffusive regime occurs for effect of the heating

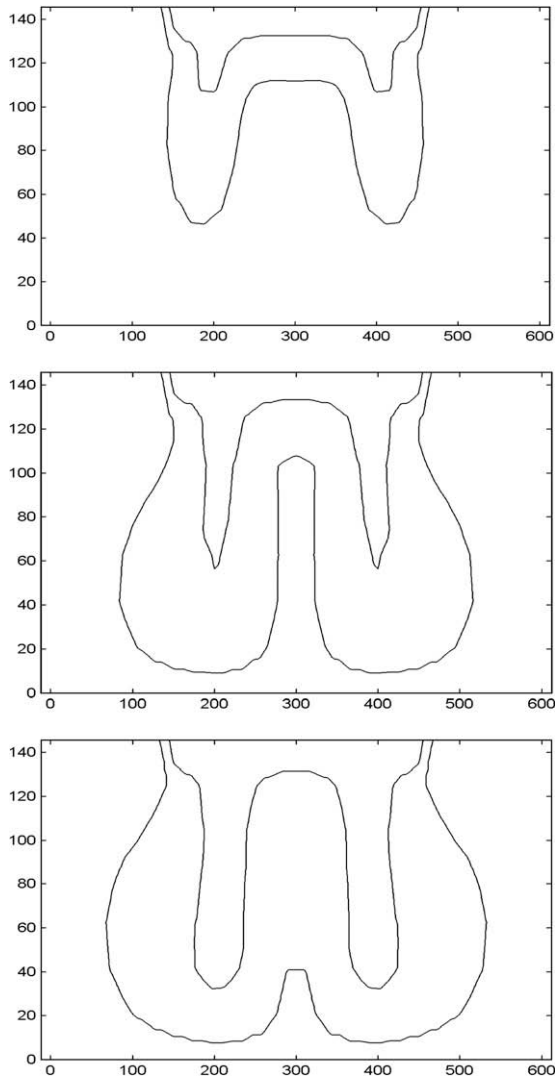

Fig. 18. Elder test: MAST FV/FE computed isopleths – level mesh 0th (4, 10 and 20 years).

(downsunk salinity is heated from below). The same mesh as the one used in the salt convection problem with 1414 elements has been used with the same time step size (1 month) (see Section 4.3.1). The maximum CFL value is 1.12. Computed isopleths of 20% and 60% of the maximum concentration and temperature contours are shown in Figs. 23(a)–23(c), 24(a)–24(c), 25(a)–25(c), Figs. 26(a) and 26(b) at the simulation times 4, 10 and 20 years, for different values of the thermal gradient ΔT.

A similar mesh refinement test has been carried out as in the salt convection test. ΔT used for these simulations is 400 K. Maximum CFL value ranges from 0.89 to 2.1, going from the coarsest to the finest mesh. In Figs. 26(a)–26(d) isopleths of 20% and 60% as well as temperature contours are shown after 20 years (results for the 1st level mesh are the ones in Fig. 25(c)). Numerical results are symmetric. Except for the coarsest mesh, mesh size effects seem to be negligible; the central flow is downwelling as previously observed for the salt convection problem, without any inversion of the flux direction. Diersch and Kolditz [16] and Diersch [17] obtained by FEFLOW asymmetric salinity profiles for high ΔT values (>200 K) and very fine mesh (9900 quadrilateral elements) (see Fig. 27).

4.4. The salt-dome test

The test case is an idealization of the flow over a salt-dome, where the geometry is greatly simplified. The attention is directed to the physics of flow of a non-homogeneous fluid, whose density is depending on the salt concentration in the salt convection problem and by both salt and temperature gradient in the thermohaline extension.

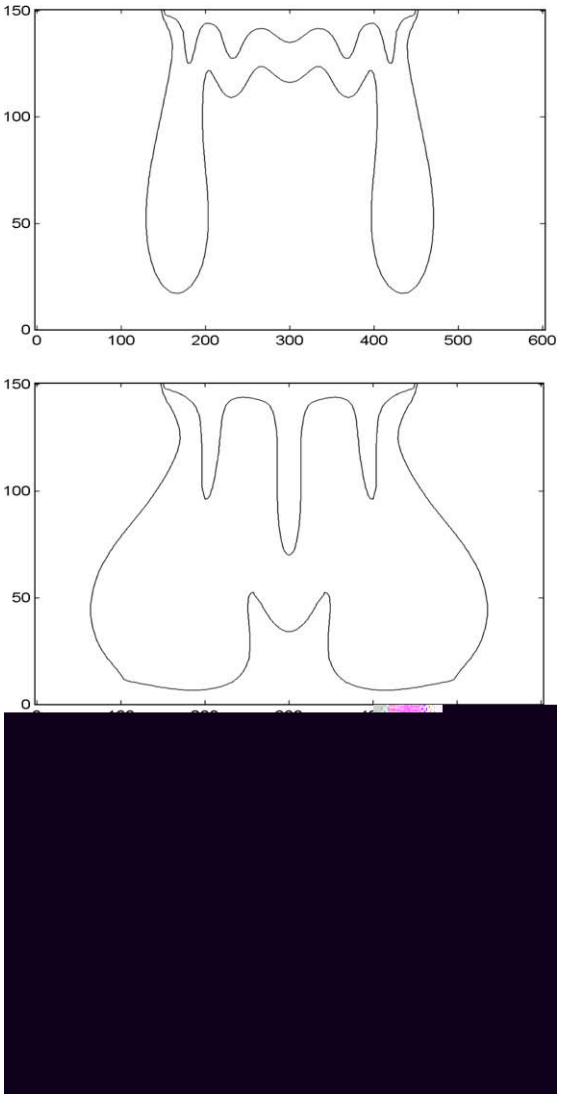

Fig. 19. Elder test: MAST FV/FE computed isopleths – level mesh 2nd (4, 10 and 20 years).

4.4.1. The salt-dome salt convection–diffusion problem

The geometry and boundary conditions of this test are shown in Fig. 28. The domain extends horizontally to 900 m and vertically to 300 m. The aquifer is assumed homogeneous and isotropic. The hydraulic head varies linearly on the top of the aquifer. The concentration is taken equal to zero on the top and on the left upstream boundary. The central part of the bottom boundary ($300 \leqslant x \leqslant 600$) represents the top of the salt-dome with relative concentration equal to 1.

Two series of simulations have been carried out, assuming this part of the bottom side either impermeable either permeable to flow. In this second case the initial pressure is assumed to remain constant during the simulation time along the permeable part of the boundary; all the other sides of the domain are impervious to the liquid and the salt. Assuming the top of the salt-dome permeable is equivalent to assume first type boundary condition for the stream function along this part of the boundary domain. This last schematization of the boundary conditions is more realistic. Parameters values are listed in Table 6.

On the permeable upper boundary salt diffusion is neglected; the concentration is assumed equal to the value of the leaving particles along the part of the boundary where a leaving flux occurs and equal to zero where an entering flux occurs. Fresh water condition and hydrostatic pressure distribution are initially assumed inside the domain.

Spatial domain has been discretized with a mesh of 1350 isosceles triangles (side 10 m) with 736 nodes. Δt is 60,000,00 s and the maximum values of the CFL number and of the Peclet number are respectively 0.93 and 23.4. Steady-state conditions are reached approximately after 400 years. In the simulations the following parameters values have been assumed: $\beta_L = 20$ m, $\beta_T = 2$ m and $D_m = 1.39d - 08$ m^2/s. Numerical results are shown in Figs. 29 and 30, respectively for the impervious

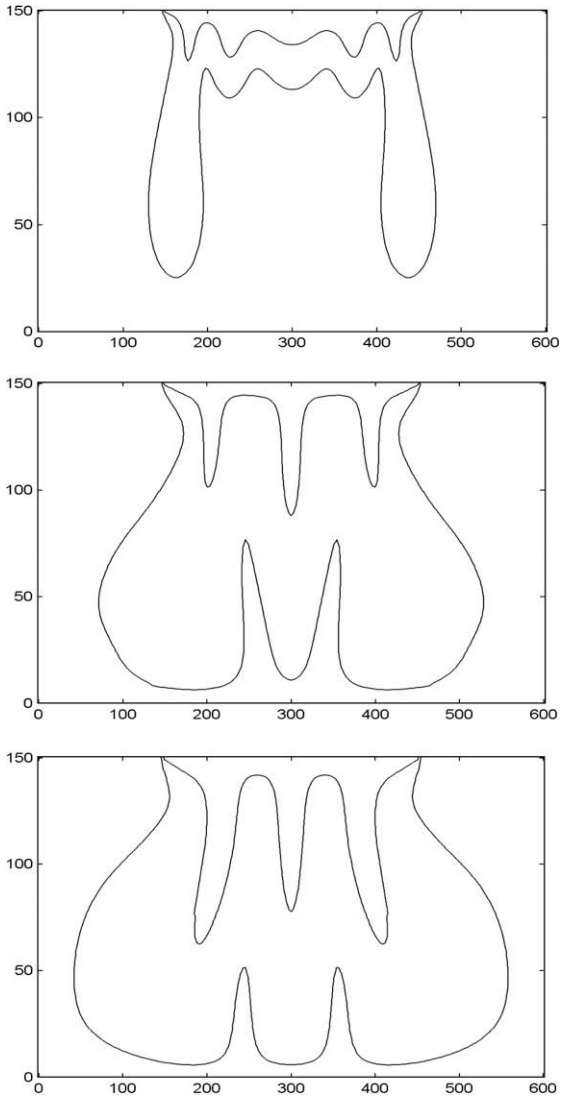

Fig. 20. Elder test: MAST FV/FE computed isopleths – level mesh 3rd (4, 10 and 20 years).

and the open bottom side. The stream lines contours provide a good visualization of the hydrodynamic problem. A freshwater region with higher velocities can be observed in the upper part of the domain where flow is essentially driven by the pressure gradient on the top side, while there is a brine pool along the bottom where flow with small velocities recirculates. The outflow of the saltwater is on the upper right-hand corner of the domain. The choice of the boundary conditions affects the numerical results. As expected, if the central bottom is assumed permeable, the velocity components normal to the boundary cause a rise of the interface brine-freshwater region. The presence of these velocity components is evident from the comparison of the stream line contours in the two cases of Figs. 29 and 30. In Fig. 31 the corresponding results obtained by NAMMU [31] and FEFLOW [17] are shown. NAMMU is a FE Galerkin code where the governing equations are given by solution mass conservation, transport equation of the solute and momentum conservation written in terms of solute mass fraction, velocity and mass fraction of the concentrated solution; both the literature models discretize the PDEs governing equations using rectangular elements: 1920 in FEFLOW simulations and 1600 for NAMMU simulations. Results of MAST FV/FE are very close to the ones of the other literature models.

Assuming the top of the salt-dome as impervious, different simulations have been carried out changing the molecular diffusion parameter and setting equal to zero the longitudinal and lateral dispersion coefficients. Results are shown in Figs. 32(a)–32(b); decreasing the value of D_m the freshwater zone moves deeper. The maximum value of the CFL numbers are approximately the same as in the previous case, while the maximum Peclet numbers are respectively 362 and 36.2 for the lowest and highest D_m coefficient. In Figs. 33(a)–33(b), the corresponding results obtained by Younes et al. [54] are

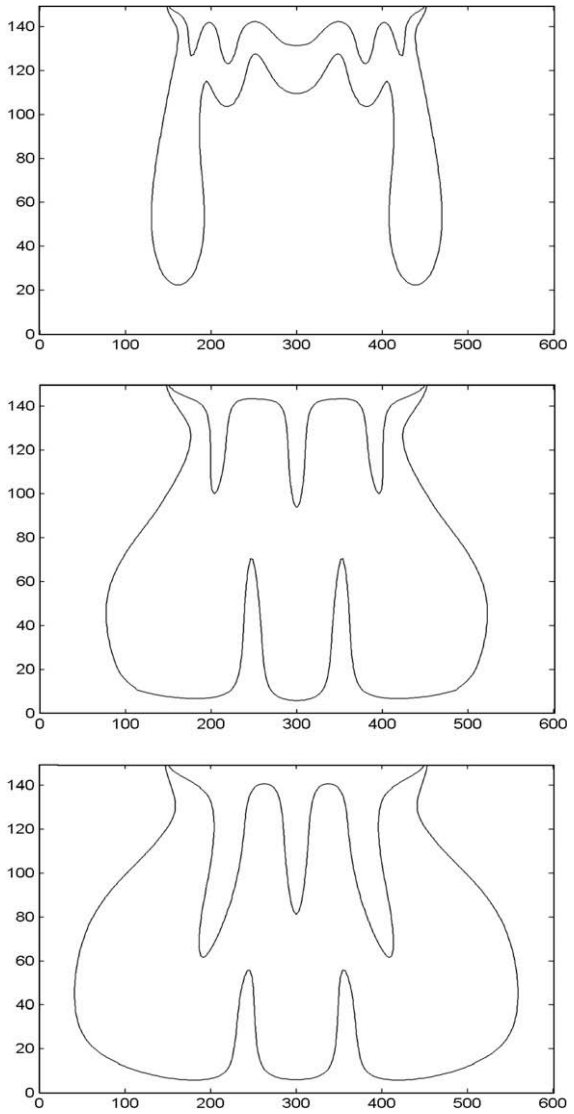

Fig. 21. Elder test: MAST FV/FE computed isopleths – level mesh 4th (4, 10 and 20 years).

Table 4
Flow direction in the central section (modified from [18]).

Authors	*Nel*				
	<1000	1000–4000	4000–16,000	16,000–64,000	>64,000
Diersch [13]	↓	–	–	–	–
Voss and Souza [53]	–	↓	–	–	–
Oldenburg and Pruess [44]	–	↓	↑	↑	–
Kolditz et al. [34]	–	↓↑	↑	↑	–
Ackerer et al. [1]	↑		↑	↑	–
Mazzia et al. [38]	–	↓	–	–	–
Oltean and Bues [45]	↑↓	↑↓	↑	↑	
Frolkovic and De Schepper [24]	–	↓	↑	–	↑↓
Diersch [18]	–	↓	↑	–	↓
MAST FV/FE	↑	↓	↓	↓	↓

shown. The authors use a mesh with 2500 quadrilateral elements. The rise of the salt front in the model by Younes et al. is higher than in MAST FV/FE, eventhough the comparison between the stream function contours is very good.

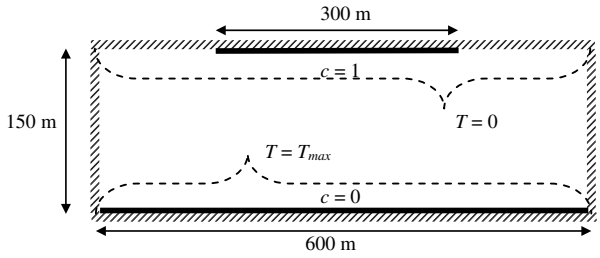

Fig. 22. Elder thermohaline test: spatial domain and boundary conditions.

Table 5
Elder thermohaline test – parameters values.

Parameter	Symbol	Units	Value
Reference concentration	C_0	(kg/m^3)	0
Temperature difference	ΔT	(K)	400
Reference temperature	T_0	(K)	0
Thermal capacity of fluid	ρc^l	(J/m^3/K)	4.2×10^6
Thermal capacity of solid	$\rho^s c^s$	(J/m^3/K)	0
Molecular diffusion coefficient	D_d	(m^2/s)	3.565×10^{-6}
Longitudinal solute dispersivity	β_L	(m)	0
Transversal solute dispersivity	β_T	(m)	0
Permeability tensor	k	(m^2)	4.845×10^{-13}
Density ratio	$\bar{\alpha}/C_s$	(–)	0.2
Thermal expansion coefficient	$\bar{\beta}$	(°C^{-1})	0.375×10^{-3}
Porosity	ε	(–)	0.1
Thermal conductivity of fluid	λ^l	(J/m/s/K)	0.65
Thermal conductivity of solid	λ^s	(J/m/s/K)	1.591
Longitudinal solute thermodispersivity	α_L	(m)	0
Transversal solute thermodispersivity	α_T	(m)	0
Reference fluid density	ρ_0	(kg/m^3)	1000
Maximum density of the solution	ρ_s	(kg/m^3)	1200
Reference fluid viscosity	μ_0	(kg/m/s)	0.001

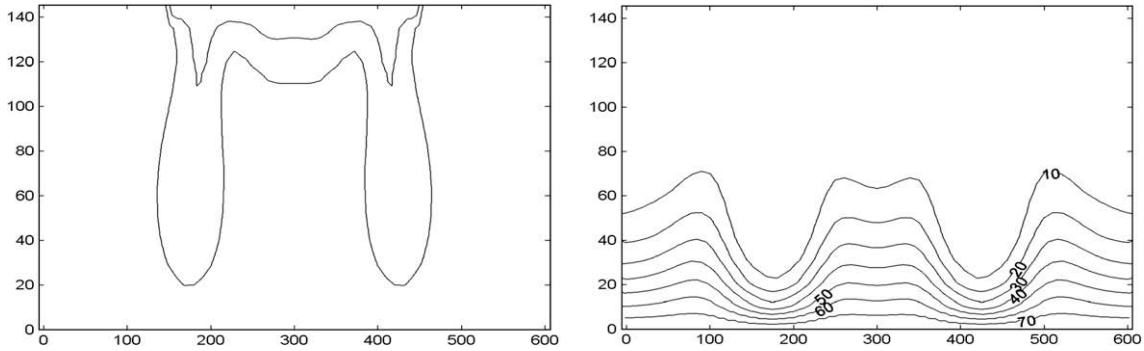

Fig. 23(a). Elder thermohaline test: MAST FV/FE isopleths, temperatures (ΔT 80 K, 4 years).

4.4.2. The salt-dome thermohaline extension

The thermohaline extension of the salt-dome problem is obtained with a superimposition of a thermal gradient acting upward that tends to destabilize the brine pool due to the arising buoyant forces. At the bottom of the aquifer a constant temperature $T = T_{max}$ is assigned, while on the top side $T = 0$ is imposed (see Fig. 34). Simulation parameters are reported in Table 7. The boundary conditions for the concentration are the same as in the convection problem. The central bottom domain is assumed impermeable. Initially, hydrostatic pressure distribution, isothermal ($T = 0$) and freshwater conditions are assumed inside the domain. In Figs. 35(a)–35(c), simulation results are shown at the simulation time 400 years for different values of the thermal gradient between the top and bottom side. The Δt is 20,000,00 s and the maximum CFL value is 0.83.

The temperature effect on the saltwater distribution remains negligible or small if compared with the single convection–diffusion problem for small thermal gradient. Increasing the ΔT, vigorous temperature influences the brine pattern result in

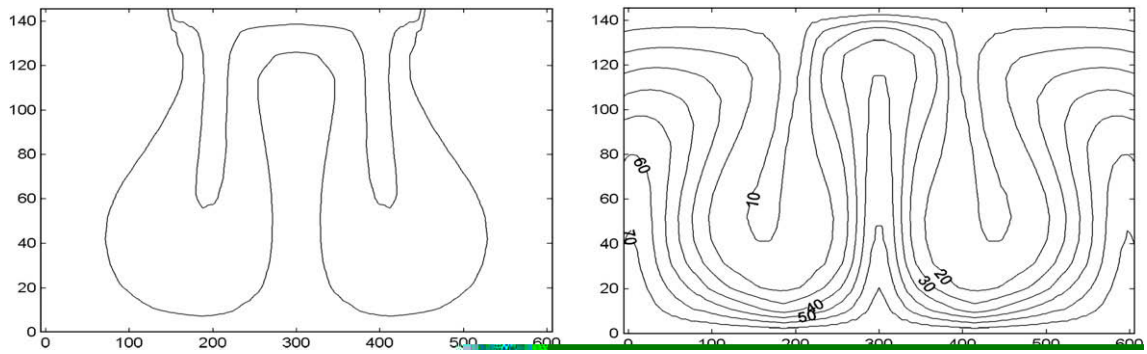

Fig. 23(b). Elder thermohaline test: MAST FV/FE isopleths, temperatures (ΔT 80 K, 10 years).

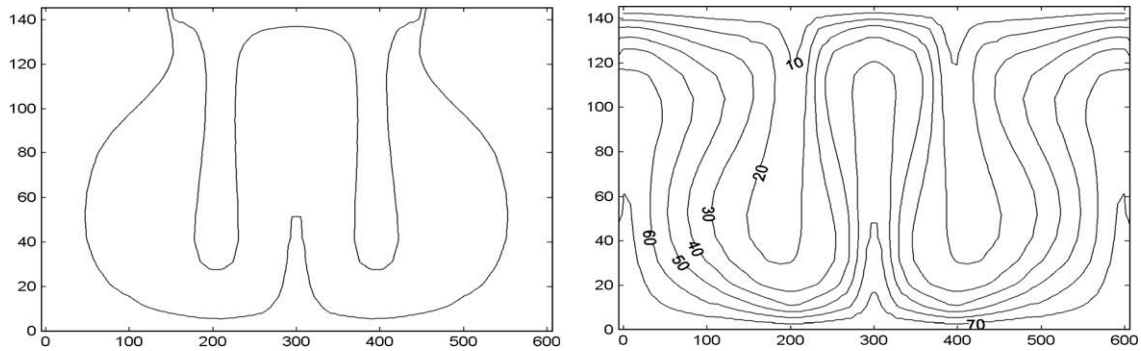

Fig. 23(c). Elder thermohaline test: MAST FV/FE isopleths, temperatures (ΔT 80 K, 20 years).

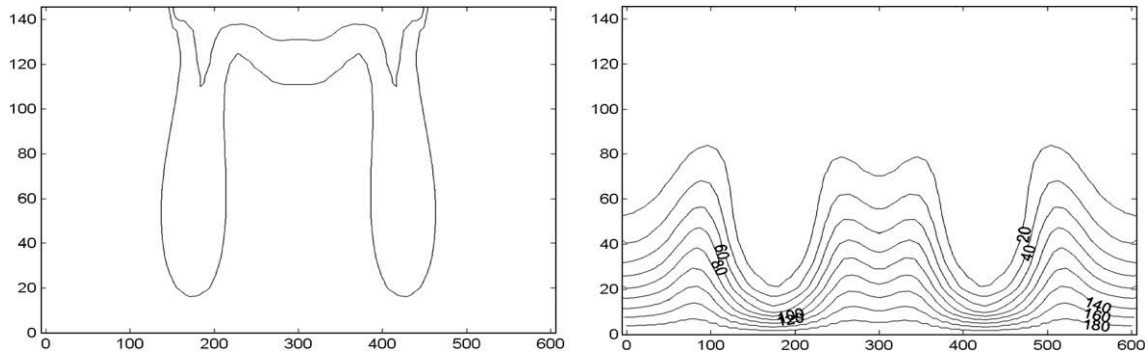

Fig. 24(a). Elder thermohaline test: MAST FV/FE isopleths, temperatures (ΔT 200 K, 4 years).

form of a 'wavy' salinity field caused by the thermal buoyancy. The 'wavy' salinity characteristics are triggered in front of the salt wedge by thermally driven eddies. As expected, this leads to an increased saltwater effluent on top of the aquifer. A similar behaviour is evident in the results computed by Diersch [17] in FEFLOW (see Figs. 36(a)–36(c).

4.5. Computational costs and sensitivity analysis

An estimation of the CPU times for the computation of the two convective and of the diffusive steps, as well as for the computation of the approximated potential, has been carried out. Results are reported in Table 8 in terms of the mean CPU times per element, for some of the tests previously shown. A processor Intel 6400 2.13 GHz has been used. The computation of the convective prediction and correction steps is the most demanding one. The CPU time required for the solution of the first diffusive system in the Ψ unknowns is about half the convective steps time, while the solution of the second diffusive system needs approximately one magnitude order less than the convective steps time. The CPU time for the computation of the approximated scalar function is similar to the one for the first diffusive system.

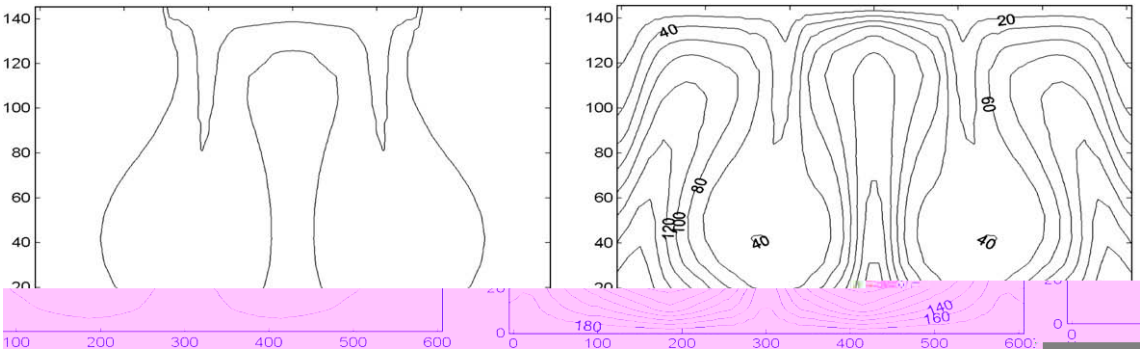

Fig. 24(b). Elder thermohaline test: MAST FV/FE isopleths, temperatures (ΔT 200 K, 10 years).

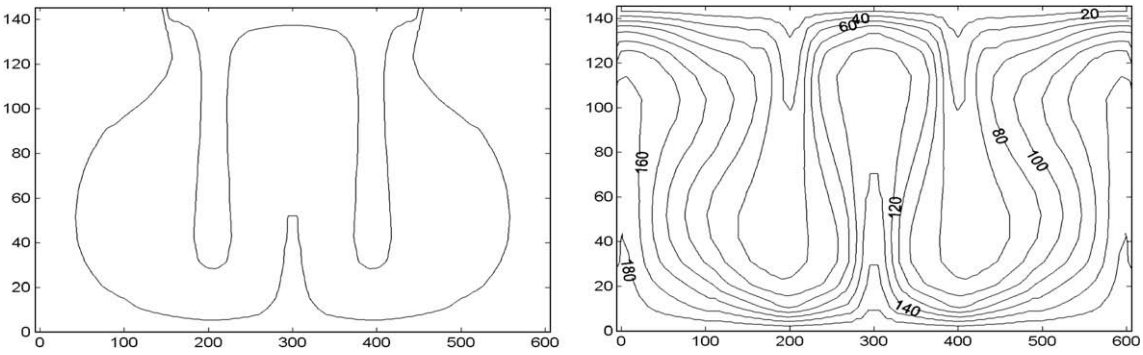

Fig. 24(c). Elder thermohaline test: MAST FV/FE isopleths, temperatures (ΔT 200 K, 20 years).

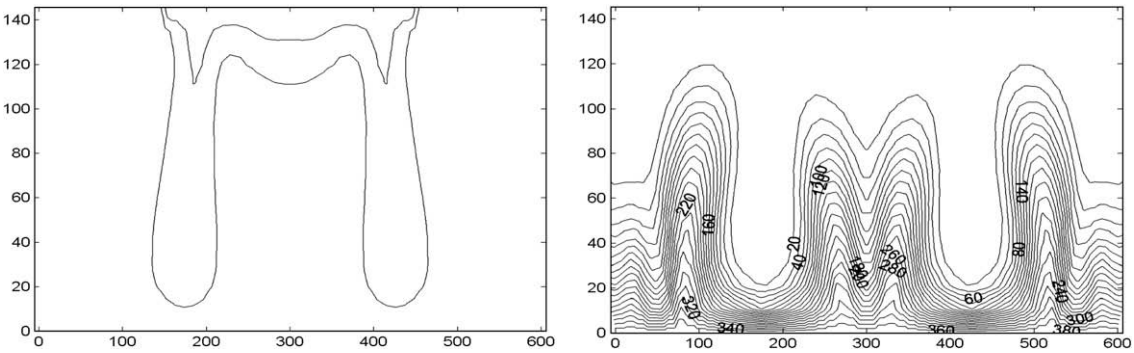

Fig. 25(a). Elder thermohaline test: MAST FV/FE isopleths, temperatures (ΔT 400 K, 4 years).

The growth of the computational time per element and per time step versus the number of elements has been investigated in order to assess the relative cost of the two diffusive correction systems and of the approximated potentials calculation. These steps require the solution of a large linear system and are the non-'explicit' component of the algorithm. The Henry test has been chosen for this investigation. A mesh with 100 isosceles triangular elements (see Fig. 7(a)) has been generated for next four refinements as described in Section 4.3.1 for the Elder salt test; the time step for the coarsest mesh is 20 s, and it has been halved at each refinement. Results are shown in Fig. 37(a). Observe that, at least up to the maximum number of elements tested in the experiments, the CPU time components relative to the convective steps is almost independent on the elements number. The small decrement of the average CPU time of the convective component can be related to the increasing CFL numbers obtained by partitioning and to the best aptitude of the algorithm to work with CFL numbers greater than one [2,3]. The two diffusive systems and the one for the approximated potential have the same structure. The differences in the CPU mean times depend on the conditioning numbers of the matrices of the three linear systems.

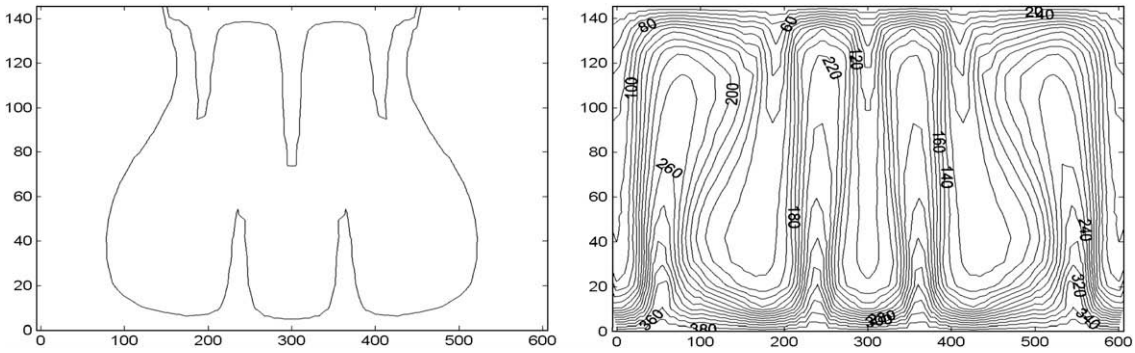

Fig. 25(b). Elder thermohaline test: MAST FV/FE isopleths, temperatures (ΔT 400 K, 10 years).

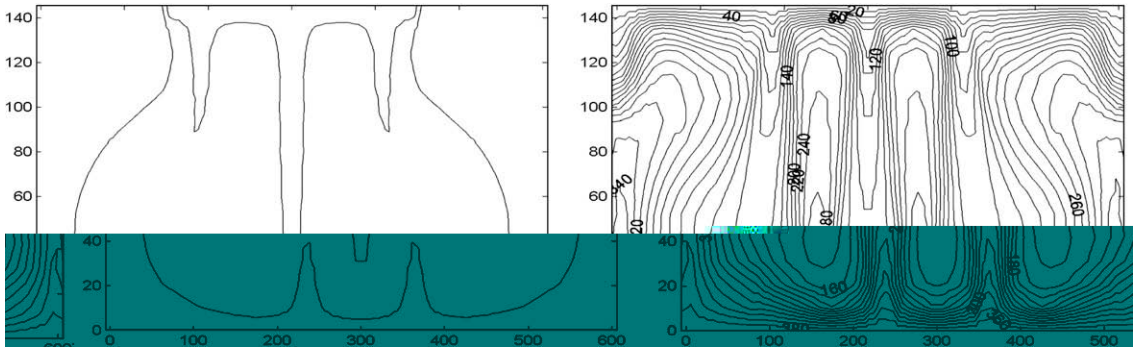

Fig. 25(c). Elder thermohaline test: MAST FV/FE isopleths, temperatures (ΔT 400 K, 20 years).

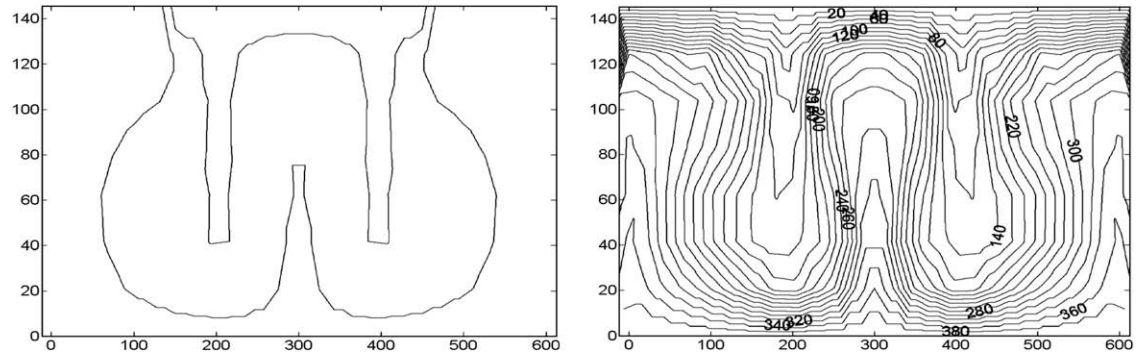

Fig. 26(a). Elder thermohaline test: MAST FV/FE isopleths, temperatures – level mesh 0th (20 years).

The growth of the CPU times with the element number have the same trend for the three systems, eventhough the condition number of the matrix of the system of the second diffusive step is lower than the condition number of the other two matrices, which values are quite similar. It is also important to observe that the growth of the mean CPU time per element with the element number is less than linear.

The same trend of the mean CPU times has been observed for the refinement test of the Elder salt convection problem (see Section 4.3.1), as reported in Fig. 37(b). It seems that the intrinsic instability of the physical and numerical processes, with a variable number of captured fingers (at least for the coarser mesh levels 0th, 1st and 2nd), as previously discussed in Section 4.3.1, does not affect the CPU mean time values. Mazzia et al. [38], analysing an analogous instable convection test case, obtained CPU times strongly affected by the instability of the problem, growing with the mesh refinement much more than linearly.

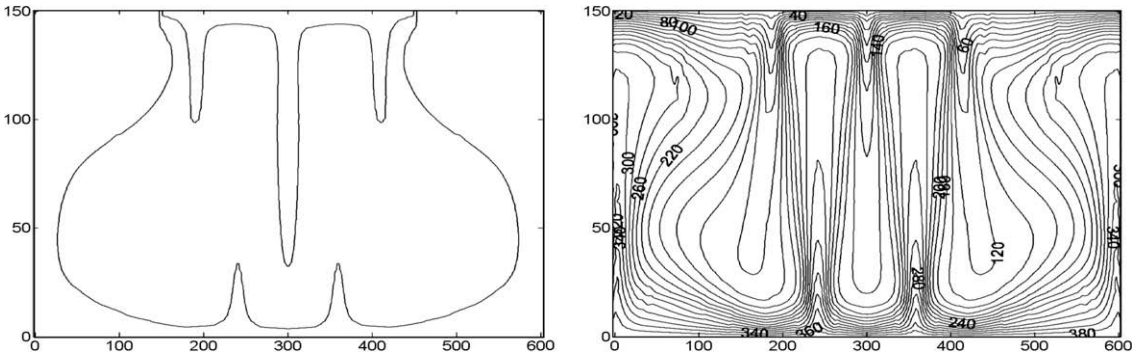

Fig. 26(b). Elder thermohaline test: MAST FV/FE isopleths, temperatures – level mesh 2nd (20 years).

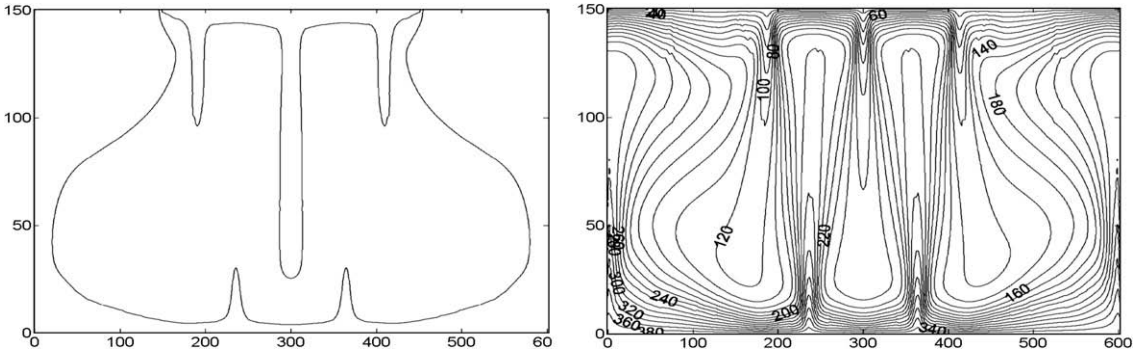

Fig. 26(c). Elder thermohaline test: MAST FV/FE isopleths, temperatures – level mesh 3rd (20 years).

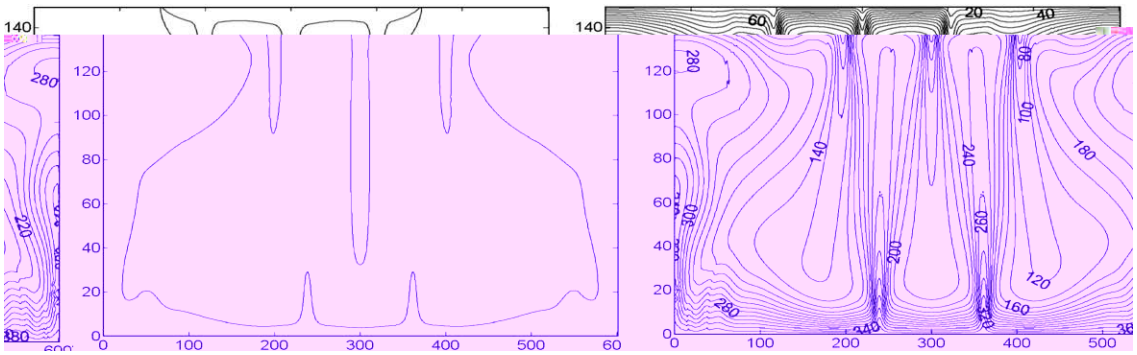

Fig. 26(d). Elder thermohaline test: MAST FV/FE isopleths, temperatures – level mesh 4th (20 years).

A second analysis has been carried out to test the sensitivity of the computational cost with respect to the size of the time step. Using the computational mesh of the Henry test with 1600 elements, the CPU mean time values for the four components have been computed increasing the size of the CFL number by changing the time step size. Results are shown in Fig. 38. The CPU mean times for the potential scalar function, as well as for both the diffusive steps are found to be almost independent from the size of the CFL number, while the growth of the computational times required for the two convective steps is much less than linear.

Finally, the sensitivity of the result accuracy with respect to the CFL number has been investigated, using the same test case with the same computational mesh. Numerical simulations have been carried out using $\Delta t = 12.5$ s and $\Delta t = 200$ s and the maximum CFL numbers are, respectively 0.66 and 10.516. The isopleths for 25%, 50% and 75% of the maximum concentration are shown in Fig. 39. These results can be also compared with the original ones, computed with $\Delta t = 25$ s and a maximum CFL number about 1.3137.

This test shows the result sensitivity with respect to the CFL number to be very small.

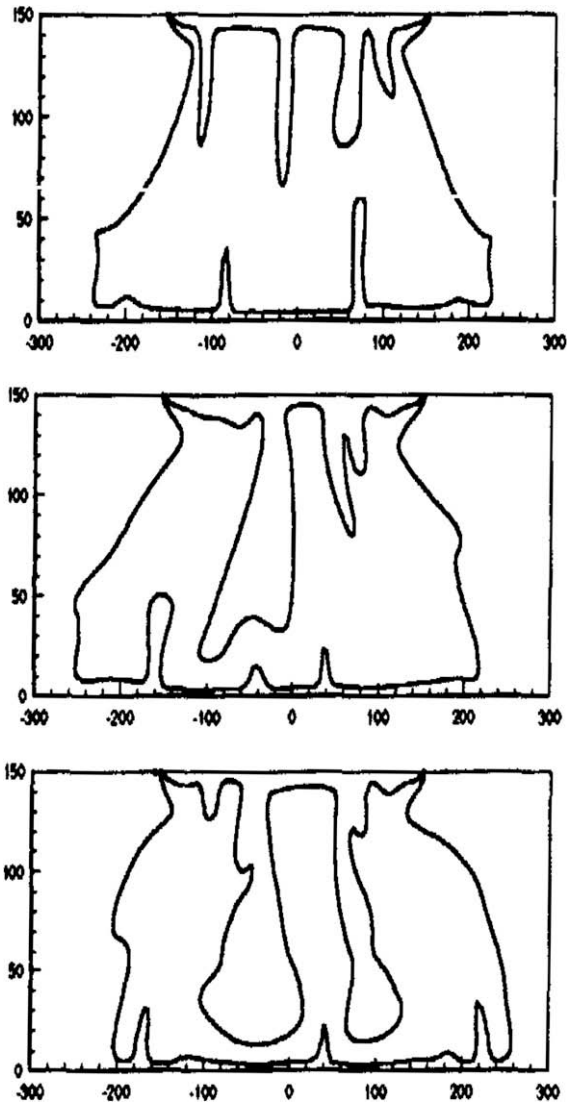

Fig. 27. Elder thermohaline test: FEFLOW [16] isopleths (10, 15 20 years from left to right, ΔT 400 K, 9900 quadrilateral elements).

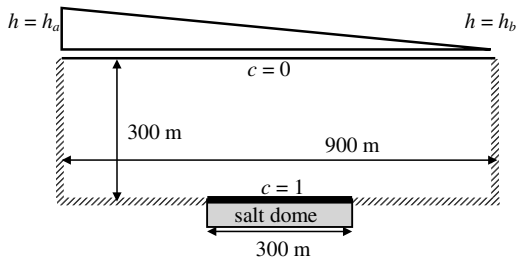

Fig. 28. Salt-dome test: spatial domain and boundary conditions.

A 1D benchmark problem solved in a 2D grid has been used to test the stability and the accuracy of the solution of the MAST FV/FE scheme within a wide range of Peclet number values. The PDE describing the movement of a tracer in a semi-infinite column has been considered; the velocity field is assumed known and constant in time, $\mathbf{q} = (1.0)$, with porosity equal to one and $\mathbf{D} = diag(D_1, D_1)$. The boundary conditions are $c = 1$ at $x = 0$ and $c = 0$ at $x = \infty$. Zero relative concentration is

Table 6
Salt-dome salt convection–diffusion test – parameters values.

Parameter	Symbol	Units	Value
Reference concentration	C_0	(kg/m^3)	0
Molecular diffusion coefficient	D_d	(m^2/s)	1.39, 5, 50 $\times$ 10^{-8}
Longitudinal solute dispersivity	β_L	(m)	20, 0, 0
Transversal solute dispersivity	β_T	(m)	2, 0, 0
Permeability tensor	k	(m^2)	4.845 $\times$ 10^{-13}
Density ratio	$\bar{\alpha}/C_s$	(–)	0.236108
Porosity	ε	(–)	0.2
Reference fluid density	ρ_0	(kg/m^3)	997
Maximum density of the solution	ρ_s	(kg/m^3)	1200
Reference fluid viscosity	μ_0	(kg/m/s)	0.00089
Freshwater head right upper corner	h_b	(m)	10.228
Freshwater head left upper corner	h_a	(m)	20.456

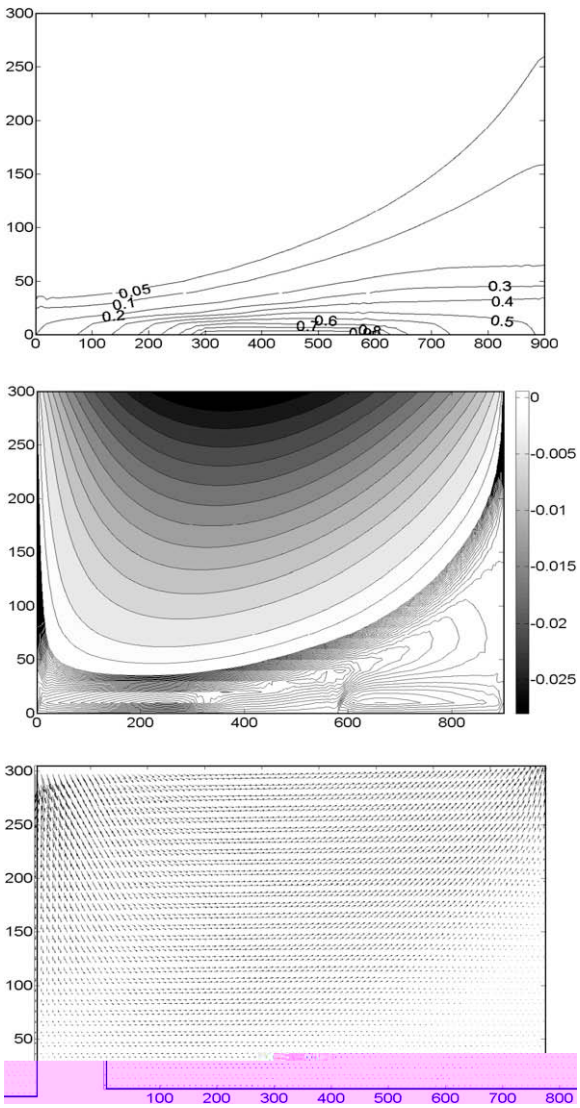

Fig. 29. Salt-dome test: MAST FV/FE computed isopleths, stream function contours and velocity field (impervious bottom; $\beta_L = 20$ m, $\beta_T = 2$ m, $D_m = 1.39d - 08$ m^2/s).

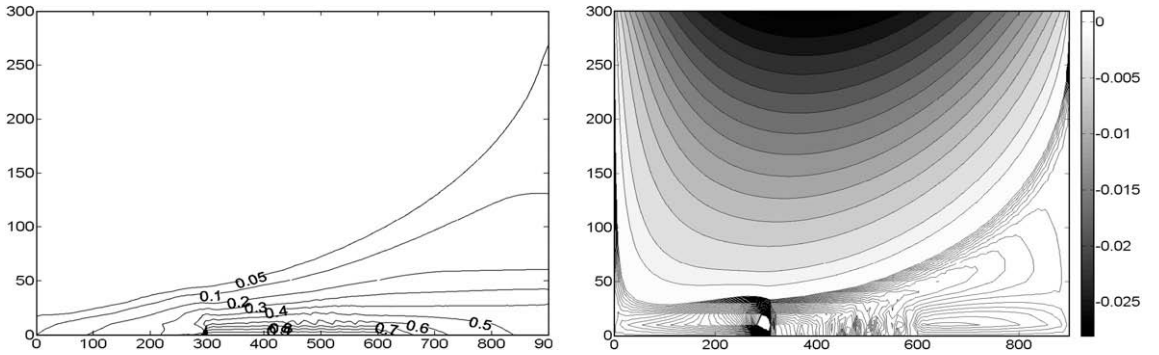

Fig. 30. Salt-dome test: MAST FV/FE computed isopleths, stream function contours and velocity field (open bottom; $\beta_L = 20$ m, $\beta_T = 2$ m, $D_m = 1.39d - 08$ m^2/s).

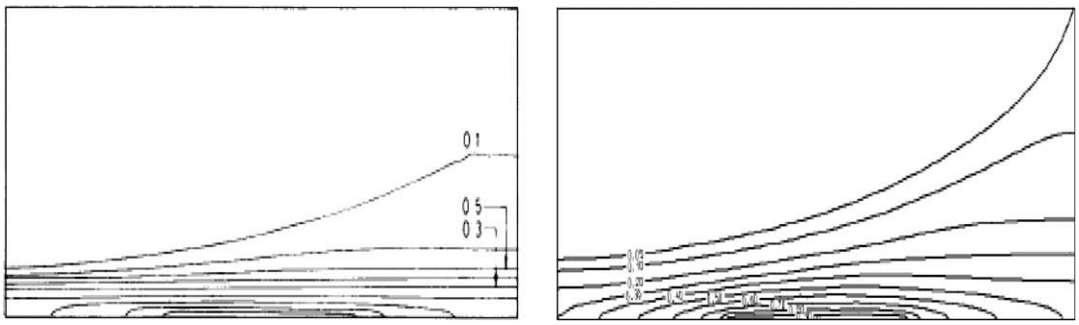

Fig. 31. Salt-dome test: NAMMU (left) [31] and FEFLOW (right) [17] computed isopleths ($\beta_L = 20$ m, $\beta_T = 2$ m, $D_m = 1.39d - 08$ m^2/s).

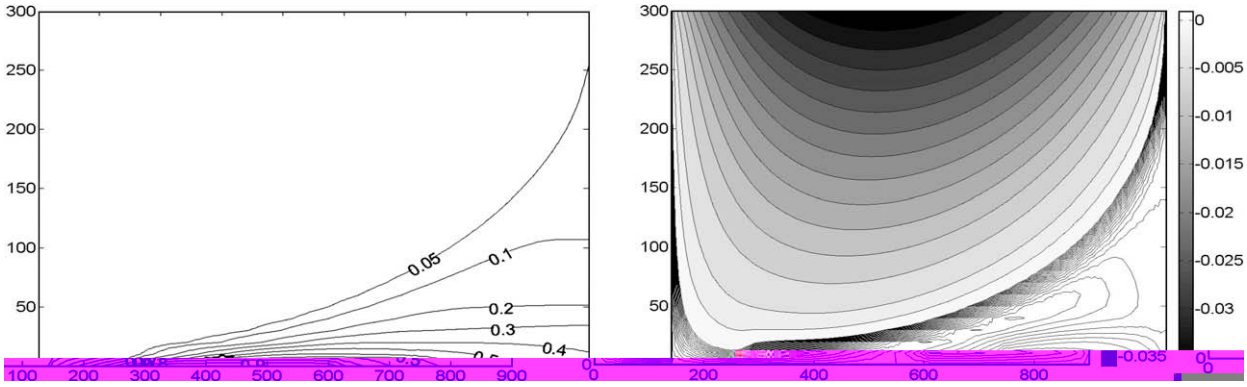

Fig. 32(a). Salt-dome test: MAST FV/FE computed isopleths and velocity field (impervious bottom; $\beta_L = 0$, $\beta_T = 0$, $D_m = 5d - 08$ m^2/s).

assumed as initial condition. The problem is simulated using a rectangular domain $[0,1] \times [0,0.025]$ discretized with 1200 triangular isosceles elements (see Fig. 7(a)). The analytical solution for this problem is [6,37]:

$$c(x,t) = \frac{1}{2}\left(erfc\frac{x - q_{x_1}t}{2\sqrt{D_1 t}} + \exp\frac{q_{x_1}x}{D_1} \cdot erfc\frac{x + q_{x_1}t}{2\sqrt{D_1 t}}\right). \tag{73}$$

The simulation time is $t = 0.7$ s. Different simulations have been carried out changing the dispersion coefficient D_1 values, for a CFL number equal to 0.75; the values of D_1, of Peclet number as well as of L_2 norm of the errors are shown in Table 9. The error and the numerical diffusion in the solution of the proposed scheme become significant when the advection terms become dominant with respect to the diffusive ones, due to the 1st spatial approximation order in the convective steps, but the solution remains always stable also for the highest Peclet numbers.

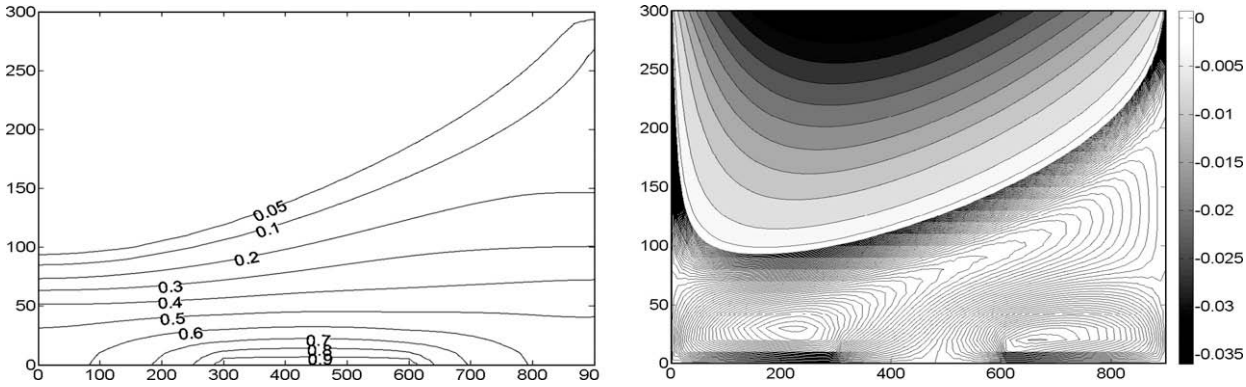

Fig. 32(b). Salt-dome test: MAST FV/FE computed isopleths and velocity field (impervious bottom; $\beta_L = 0$, $\beta_T = 0$, $D_m = 5d - 07$ m^2/s).

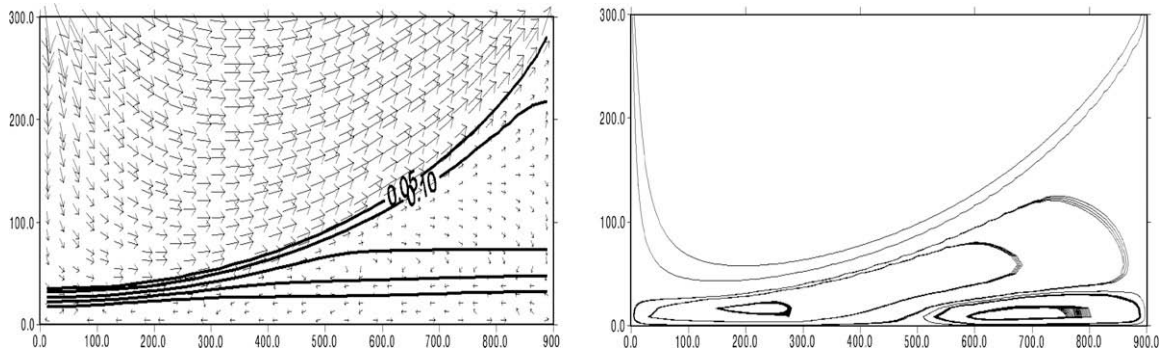

Fig. 33(a). Salt-dome test: Younes et al. [54] computed isopleths and stream function contours (impervious bottom; $\beta_L = 0$, $\beta_T = 0$, $D_m = 5d - 08$ m^2/s).

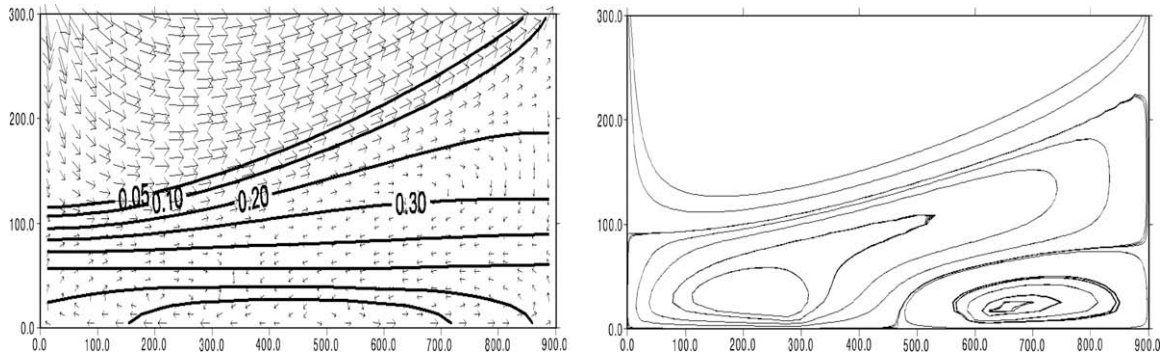

Fig. 33(b). Salt-dome test: Younes et al. [54] computed isopleths and stream function contours (impervious bottom; $\beta_L = 0$, $\beta_T = 0$, $D_m = 5d - 07$ m^2/s).

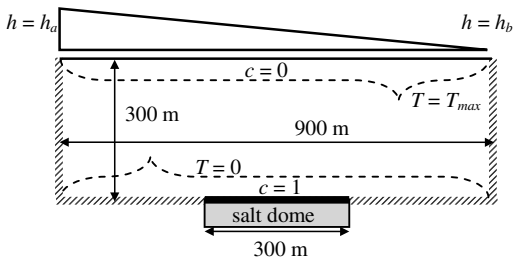

Fig. 34. Salt-dome thermohaline test: domain and boundary conditions.

Table 7
Salt-dome thermohaline test – parameters values.

Parameter	Symbol	Units	Value
Reference concentration	C_0	(kg/m^3)	0
Temperature difference	ΔT	(K)	80, 133.33, 200
Reference temperature	T_0	(K)	1
Thermal capacity of fluid	ρc^l	(J/m^3/K)	4.2×10^6
Thermal capacity of solid	$\rho^s c^s$	(J/m^3/K)	2.52×10^{-6}
Molecular diffusion coefficient	D_d	(m^2/s)	1.39×10^{-8}
Longitudinal solute dispersivity	β_L	(m)	20
Transversal solute dispersivity	β_T	(m)	2
Permeability tensor	k	(m^2)	4.845×10^{-13}
Density ratio	$\bar{\alpha}/C_s$	(–)	0.236108
Thermal expansion coefficient	$\bar{\beta}$	(°C^{-1})	5×10^{-4}
Porosity	ε	(–)	0.2
Thermal conductivity of fluid	λ^l	(J/m/s/K)	0.65
Thermal conductivity of solid	λ^s	(J/m/s/K)	3
Longitudinal solute thermodispersivity	α_L	(m)	20
Transversal solute thermodispersivity	α_T	(m)	2
Reference fluid density	ρ_0	(kg/m^3)	997
Maximum density of the solution	ρ_s	(kg/m^3)	1200
Reference fluid viscosity	μ_0	(kg/m/s)	0.00089
Freshwater head right upper corner	h_b	(m)	10.228
Freshwater head left upper corner	h_a	(m)	20.456

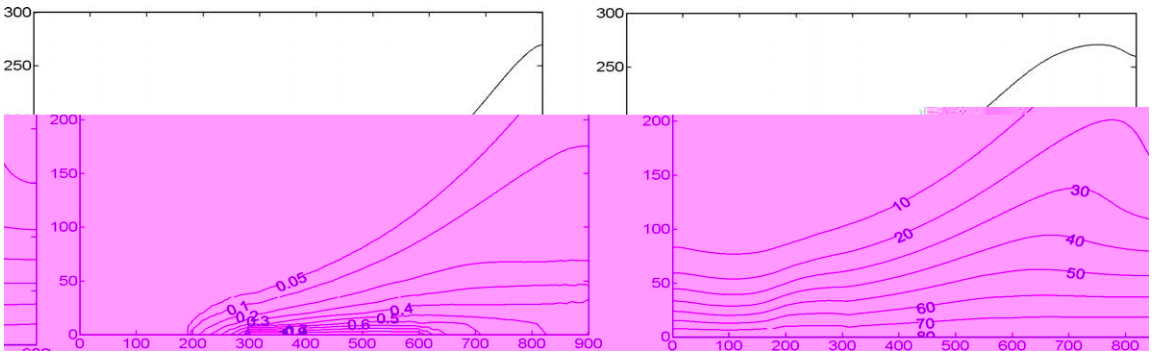

Fig. 35(a). Salt-dome thermohaline test: MAST FV/FE computed isopleths, temperatures and stream function contours (ΔT 80 K).

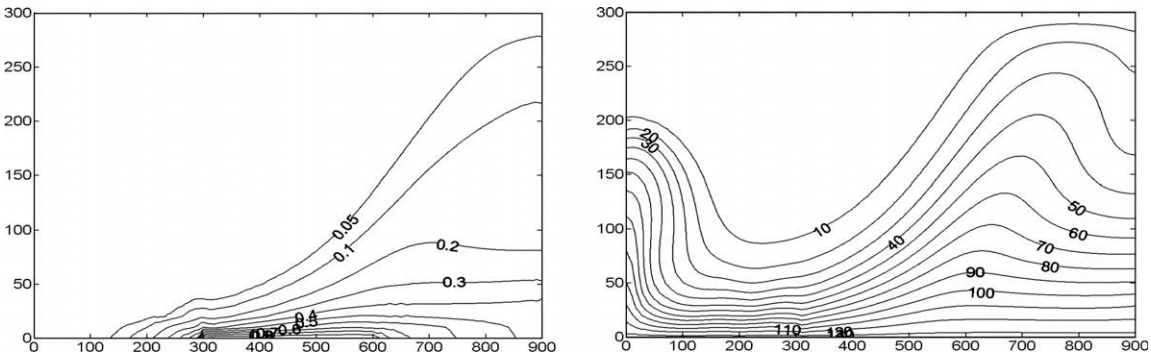

Fig. 35(b). Salt-dome thermohaline test: MAST FV/FE computed isopleths, temperatures and stream function contours (ΔT 133.33 K).

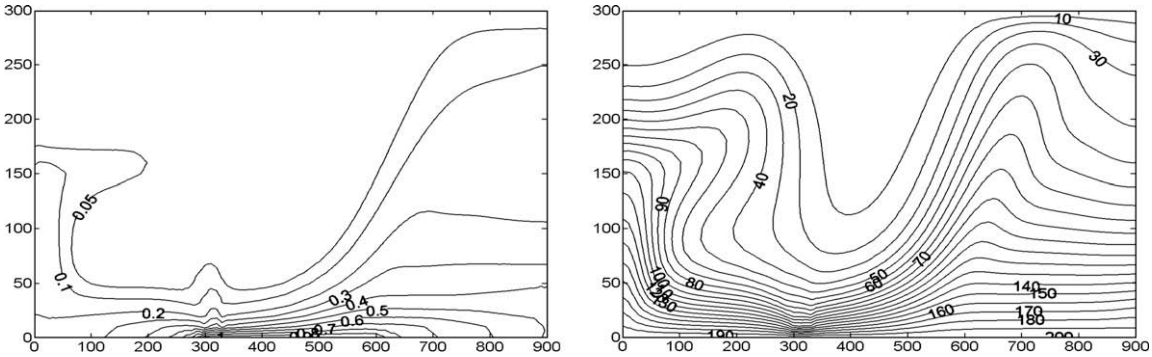

Fig. 35(c). Salt-dome thermohaline test: MAST FV/FE computed isopleths, temperatures and stream function contours (ΔT 200 K).

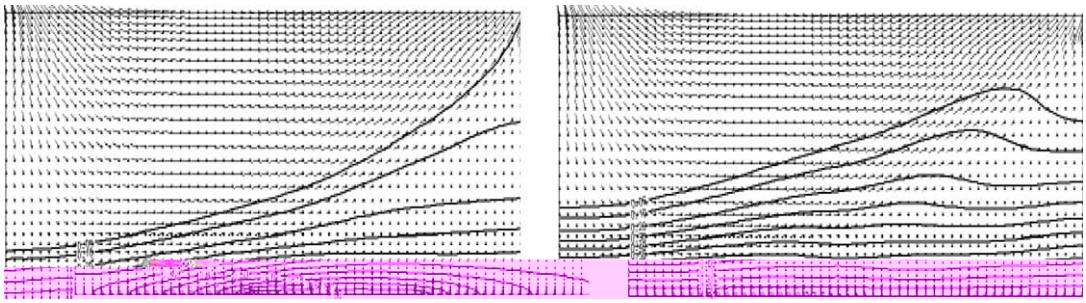

Fig. 36(a). Salt-dome thermohaline test: FEFLOW computed isopleths, temperatures and velocity field (ΔT 80 K) [17].

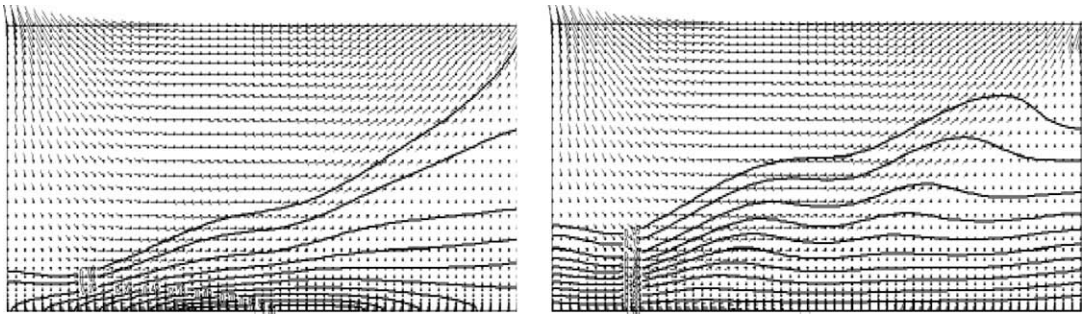

Fig. 36(b). Salt-dome thermohaline test: FEFLOW computed isopleths, temperatures and velocity field (ΔT 133.33 K) [17].

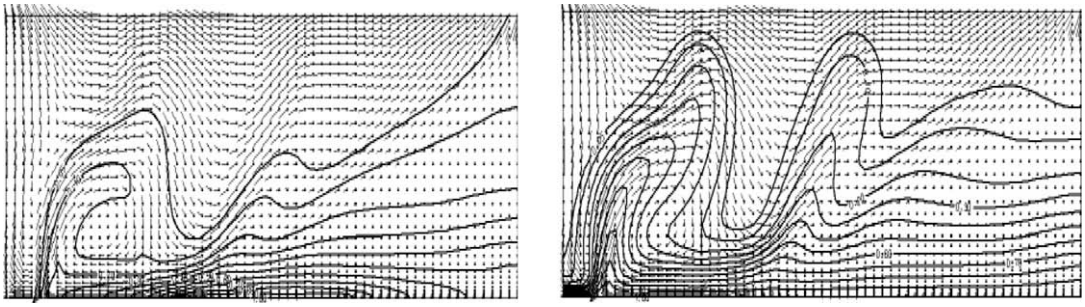

Fig. 36(c). Salt-dome thermohaline test: FEFLOW computed isopleths, temperatures and velocity field (ΔT 200 K) [17].

Table 8
Mean CPU time values.

Test	N_e	Approximately potential	Convective	Diffusive SF	Diffusive C
Henry	1600	1.2728E−05	6.16862E−05	9.01693E−06	3.14128E−06
Elder	1414	8.0114E−06	8.13572E−05	6.99847E−06	2.90068E−06
Salt-dome	5400	1.81E−05	6.12E−05	1.76E−05	2.91E−06

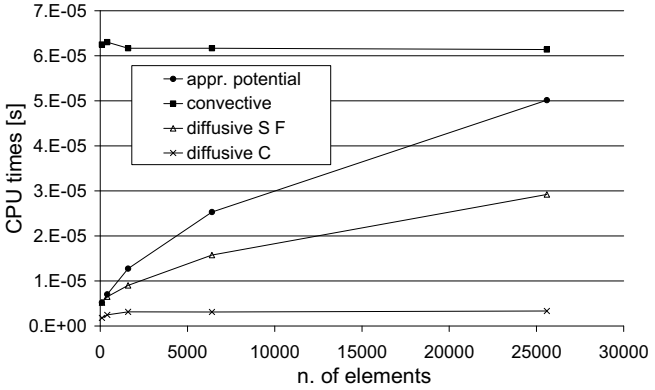

Fig. 37(a). Mean CPU times (Henry test).

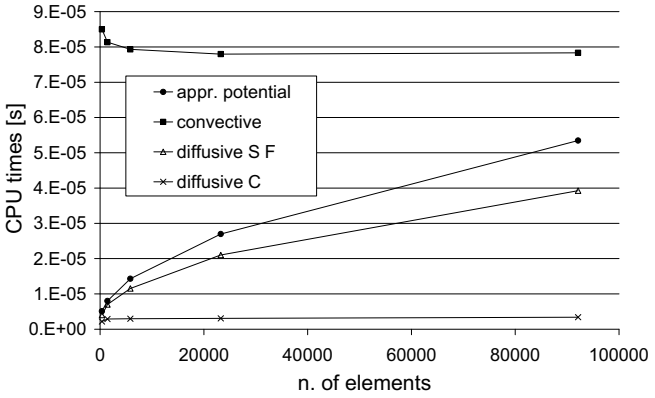

Fig. 37(b). Mean CPU times (Elder salt convection test).

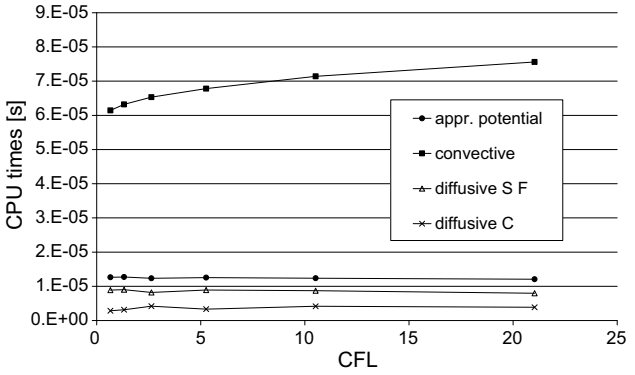

Fig. 38. Effects of the CFL number on the CPU times (Henry test).

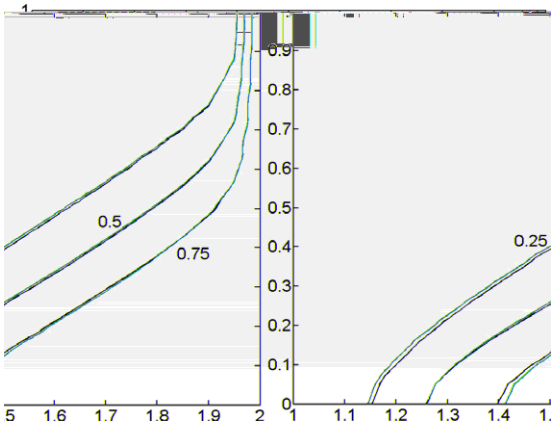

Fig. 39. Henry test: MAST FV/FE computed isopleths with different Δt (*Nel* 1600).

Table 9
Peclet numbers and L_2 norms of the errors for different diffusion coefficients.

D_1	Peclet	L_2
2.00E−02	0.32	1.47E−03
1.00E−02	0.645	2.38E−03
5.00E−03	1.29	3.75E−03
1.00E−03	6.45	8.58E−03
5.00E−04	12.9	1.06E−02
1.00E−04	64.55	1.46E−02
5.00E−05	129.1	1.57E−02

5. Conclusions

A novel methodology for the simulation of thermohaline processes in variable-density flow field has been presented. The previously proposed MAST procedure is applied for the solution of these groundwater flow and transport problems. The study is limited to 2D cases.

Mass-based stream function is used to describe the flow field. The method splits the solution of the convective components, solved by means of a FV marching in space and time (MAST) method, from the diffusive ones, solved by means of a standard Galerkin FE method.

The main advantage of the algorithm is that the first and the second non-linear sub-problem can be solved locally element after element, without any stability restriction on the size of the time step.

The proposed procedure is validated using different literature tests and results seem in good agreement with the corresponding ones provided by other numerical codes. The method shows stability also for CFL values greater than 1 in a wide range of Peclet number, as well as robustness with respect to the mesh density, also for tests subject to initial instability (the Elder problem).

An analysis of the CPU mean time values has been also carried out. The computation of both convective components is the most demanding one, but remains approximately the same per element increasing the element number; the computation of the approximated potential and of the diffusive systems are, respectively one half and about 1 magnitude order less than the one for the convective steps, and the increment of the CPU specific time with respect to the element number is much less than linear.

The present procedure presents the following advantages with respect to other FV/FE methods available in the literature (see for example [37–39]): (1) the same time step can be used for both the convective and the diffusive correction steps, because of the unconditional stability of the MAST procedure; (2) refining the computational mesh, the growth of the CPU time against the number of elements is much less than linear.

MAST FV/FE scheme can be extended to the study of 3D density-dependent groundwater problems by writing the mass conservation equation of the liquid phase in terms of the piezometric head h (or fluid pressure p) and computing the velocity components q_i ($i = 1,2,3$) as function of the spatial gradients of h (or p) known at the end of the previous time step.

One of the main disadvantages of the actual version of the proposed model respect to other literature FV/FE methods models [37–39] is that, since the diffusive correction step is solved by means of a standard Galerkin FE scheme, the dual mesh has to be used also in the convective steps. The use of other FE methods that honour the mass continuity inside the elements (as the MHFE [37–39]) could help in further reducing the algorithm computational time.

Appendix 1

The finite element formulation for the pollutant (heat) transport problem in the correction step

The following dissertation concerning the FE formulation for the pollutant transport problem is analogous for the heat transport. For brevity, only the first one will be studied.

Given the following PDE (the second in system 24):

$$\varepsilon\frac{\partial C}{\partial t}-\nabla\cdot(\mathbf{D}^{k+1/2}\nabla C)=-\nabla\cdot(\mathbf{D}\nabla C)^{k}, \tag{A.1}$$

in the unknown C, the FE approximation of Eq. (A.1) is:

$$\int_{\Omega}\varepsilon\frac{\partial\widehat{C}}{\partial t}w_m d\Omega-\int_{\Omega}\frac{\partial}{\partial x_i}\left(D_{ij}^{k+1/2}\frac{\partial\widehat{C}}{\partial x_j}\right)w_m d\Omega=-\int_{\Omega}\frac{\partial}{\partial x_i}\left(D_{ij}^{k}\frac{\partial\widehat{C}^{k}}{\partial x_j}\right)w_m d\Omega\quad m=1,\ldots,N\quad i,j=1,2, \tag{A.2}$$

where Ω is the spatial integration domain, w_m is the Galerkin shape function and $\widehat{C}$ is the interpolation function, defined as

$$\widehat{C}(x_1,x_2,t)=\sum_{m=1,N}w_m(x_1,x_2)C_m(t), \tag{A.3}$$

where C_m are the unknown nodal values.

Assuming a constant value for the porosity ε along the domain, applying the Green's lemma to the second integral on the l.h.s. and to the integral on the r.h.s. of Eq. (A.2), one gets:

$$\begin{aligned}&\sum_{e_T=1,Nel}\left(\varepsilon\sum_{m=1,N}\int_{\Omega_e}w_n w_m\frac{dC_m}{dt}d\Omega\right)+\sum_{e_T=1,Nel}\int_{\Omega}\left(D_{ij}^{k+1/2}\frac{\partial w_n}{\partial x_i}\frac{\partial w_m}{\partial x_j}\right)C_m d\Omega-\int_{L_\Omega}w_n\left(D_{ij}^{k+1/2}\frac{\partial\widehat{C}}{\partial x_i}\right)dL\\&=\sum_{e_T=1,Nel}\int_{\Omega}\left(D_{ij}^{k}\frac{\partial w_n}{\partial x_i}\frac{\partial w_m}{\partial x_j}\right)C_m^k d\Omega-\int_{L_\Omega}w_n\left(D_{ij}^{k}\frac{\partial\widehat{C}^{k}}{\partial x_i}\right)dL\quad n=1,\ldots,N,\end{aligned} \tag{A.4}$$

where L_Ω is the line boundary of Ω and the integral lines on the l.h.s. and on the r.h.s. represent the diffusive boundary fluxes; these are assumed equal to zero along both impervious and pervious boundary sides, as specified in the section on the boundary conditions for the second correction systems (see Section 3.7.2).

The first term on the l. h. s. of Eq. (A.4) is the capacity term. In order to improve stability (Gambolati, 1994), the approximations:

$$\sum_{e_T=1,Nel}\left(\sum_{m=1,N}\int_{\Omega_e}w_n w_m\frac{dC_m}{dt}d\Omega\right)\cong\varepsilon\frac{C_m^{k+1}-C_m^{k+1/2}}{\Delta t}\Omega^m, \tag{A.5}$$

are made, where Ω^m is the area of the polygon around node m delimited by the centers of mass. To balance the mass error introduced by changing the first to second spatial approximation order, moving from the prediction to the correction step, the further approximation is made in Eq. (A.4):

$$\sum_{e_T=1,Nel}\left(\sum_{m=1,N}\int_{\Omega_e}w_n w_m\frac{dC_m}{dt}d\Omega\right)\cong\varepsilon\frac{C_m^{k+1}-C_m^{k+1/2}}{\Delta t}\sigma^m, \tag{A.6}$$

where σ^m is the area of the polygon delimited by the axis centers.

References

[1] P. Ackerer, A. Younes, R. Mosé, Modeling variable-density flow and solute transport in porous medium: 1. Numerical model and verification, Trans. Porous Media 35 (3) (1999) 345–373.
[2] C. Aricò, T. Tucciarelli, MAST solution of advection problems in irrotational flow fields, Adv. Water Resour. 30 (2007) 665–685, doi:10.1016/j.advwatres.2006.03.007.
[3] C. Aricò, T. Tucciarelli, A marching in space and time (MAST) solver of the shallow water equations. Part I: The 1D case, Adv. Water Resour. 30 (2007) 1236–1252, doi:10.1016/j.advwatres.2006.11.003.
[4] C. Aricò, C. Nasello, T. Tucciarelli, A marching in space and time (MAST) solver of the shallow water equations. Part II: The 2D case, Adv. Water Resour. 30 (2007) 1253–1271, doi:10.1016/j.advwatres.2006.11.004.
[5] A. Bascià, T. Tucciarelli, An explicit unconditionally stable numerical solution of the advection problem in irrotational flow fields, Water Resour. Res. 40 (6) (2004) W06501, doi:10.1029/2003WR002646.
[6] J. Bear, Hydraulics of Groundwater, McGraw-Hill, New York, 1979.
[7] V. Casulli, Eulerian–Lagrangian methods for hyperbolic and convection dominated parabolic problems, in: Computational Methods for Non-linear Problems, Pineridge, Swansea, 1987, pp. 239–269.
[8] C.N. Dawson, Godunov-mixed methods for immiscible displacement, Int. J. Numer. Meth. Fluid 11 (7) (1990) 835–847.
[9] C.N. Dawson, Godunov-mixed methods for advective flow problems in one space dimension, SIAM J. Numer. Anal. 28 (5) (1991) 1282–1309.
[10] C.N. Dawson, Godunov-mixed methods for advection–diffusion equations problems in one space dimension, SIAM J. Numer. Anal. 30 (5) (1993) 1315–1332.

[11] C.N. Dawson, High resolution upwind-mixed finite-elements methods for advection–diffusion equations with variable time-stepping, Numer. Meth. PDE 11 (1995) 525–538.
[12] G. De Josseling de Jong, Generating functions in the theory of flow through porous media, in: R.J.M. De Wiest (Ed.), Flow Through Porous Media, Academic press, San Diego, California, 1969.
[13] H.-J.G. Diersch, Primitive variables finite-element solutions of free convection flows in porous media, Zschr. Angew. Math. Mech. (ZAMM) 61 (1981) 325–337.
[14] H.-J.G. Diersch, Finite-element modeling of recirculating density-driven saltwater intrusion process in groundwater, Adv. Water Resour. 11 (1988) 25–43.
[15] H.-J.G. Diersch, Interactive, graphic-based finite-element simulation systems – FEFLOW – for modelling groundwater flow and contaminant transport process, edited by WASY, Berlin, 1994.
[16] H.-J.G. Diersch, O. Kolditz, Coupled groundwater flow and transport: 2. Thermohaline and 3D convection systems, Adv. Water Resour. 21 (1998) 401–425.
[17] H.-J.G. Diersch, FEFLOW finite-element subsurface flow and transport simulation system – user's manual/reference manual/white papers. Release 5.0, edited by WASY Ltd., Berlin, 2002.
[18] H.-J.G. Diersch, FEFLOW finite-element subsurface flow and transport simulation system, white papers II, edited by WASY Ltd., Berlin, 2002.
[19] H.-J.G. Diersch, O. Kolditz, Variable-density flow and transport in porous media: approaches and challenges, Adv. Water Resour. 25 (2002) 899–944.
[20] J.W. Elder, Steady free convection in a porous medium heated from below, J. Fluid Mech. 27 (1967) 29–48.
[21] J.W. Elder, Transient convection in a porous medium, J. Fluid Mech. 27 (1967) 609–623.
[22] D.G. Evans, J.P. Raffensperger, On the stream function for density-variable groundwater flow, Water Resour. Res. 28 (8) (1992) 2141–2145.
[23] E.O. Frind, Simulation of long-term transient density-dependent transport in groundwater, Adv. Water Resour. 5 (1982) 73–88.
[24] P. Frolkovic, H. De Schepper, Numerical modelling of convection dominated transport with density-driven flow in porous media, Adv. Water Resour. 24 (1) (2001) 63–72.
[25] G. Galeati, G. Gambolati, On boundary conditions and point sources in the finite-element integration of the transport equation, Water Resour. Res. 25 (5) (1989) 847–856.
[26] G. Galeati, G. Gambolati, S. Neumann, Coupled and partially coupled Eulerian–Lagrangian model of freshwater–seawater mixing, Water Resour. Res. 28 (1) (1992) 149–165.
[27] W. Guo, G.D. Bennett, SEAWAT Version 1.1: A Computer Program for Simulations of Groundwater Flow of Variable-Density, Fort Myers, Missimer International Inc., Florida, 1998.
[28] W. Guo, C.D. Langevin, User's guide to SEAWAT: a computer program for the simulation of three-dimensional variable-density groundwater flow. USGS Techniques of Water Resources Investigations Book 6, USGS, 2002 (Chapter A7).
[29] H.R. Henry, Effects of dispersion on salt enrichment in coastal aquifers, in: US Geological Survey Water Supply Paper 1613-C, Sea Water in Coastal Aquifers, 1964, pp. C70–C84.
[30] H.R. Henry, J.B. Hilleke, Exploration of multiphase fluid flow in a saline aquifer system affected by geothermal heating, Bureau of Engineering Research, Report No. 150–118, University of Alabama, US Geological Survey Contract No. 14-08-0001-12681, National Technical Information Service Publication No. PB234233, 105, 1972.
[31] W. Herbert, C.P. Jackson, D.A. Lever DA, Coupled groundwater flow and solute transport with fluid density strongly dependent on concentration, Water Resour. Res. 24 (1988) 1781–1795.
[32] J.D. Hughes, W.E. Sandford, SUTRA–MS, A version of SUTRA modified to simulate heat and multiple-solute transport, Reference Manual, US Department of the interior, US Geological Survey, 2004.
[33] P.S. Huyakorn, C. Taylor, Finite-element models for coupled groundwater flow and convective dispersion, in: W.G. Gray, et al. (Ed.), Proceedings of the 1st International Conference Finite-elements in Water Resource, Princeton University, Pentech Press, London, vol. 1, 1976, pp. 131–151.
[34] O. Kolditz, R. Ratke, H.J.G. Diersch, W. Zielke, Coupled groundwater flow and transport: 1. Verification of variable-density flow and transport models, Adv. Water Resour. 21 (1998) 27–46.
[35] O. Kolditz, A. Habbar, R. Kaiser, T. Rother, C. Thorenz, ROCKFLOW – theory and user's manual. Release 3.6, Institute of Fluid Mechanics, University of Hannover, Germany, 2001.
[36] K.P. Kröhn, Simulation von Transportvorgängen im klüftigen Gestein mit der Methode der Finiten-Elemente. Bericht Nr. 29/1991, Institut für Strömungsmechanik, Universität Hannover, Dissertation, 1991.
[37] A. Mazzia, L. Bergamaschi, M. Putti, A time-splitting technique for the advection–dispersion equation in groundwater, J. Comput. Phys. 157 (1) (2000) 181–198.
[38] A. Mazzia, L. Bergamaschi, M. Putti, On the reliability of numerical solutions of brine transport in groundwater: analysis of infiltration from a salt-lake, Transp. Porous Media 43 (2001) 65–86.
[39] A. Mazzia, M. Putti, Higher order Godunov-mixed methods on tetrahedral meshes for density driven flow simulations in porous media, J. Comput. Phys. 208 (2005) 154–174, doi:10.1016/j.jcp.2005.01.029.
[40] Nag Library Manual, 2005. <http://www.nag.co.uk/numeric/fl/manual/html/mark21.html>.
[41] C. Nasello, T. Tucciarelli, A dual multi-level urban drainage model, ASCE J. Hydr. Eng. 131 (9) (2005) 743–747.
[42] S.P. Neumann, A Eulerian–Lagrangian numerical scheme for the dispersion convection equation using conjugate space time grids, J. Comput. Phys. 41 (1981) 270–294.
[43] V. Noto, T. Tucciarelli, The DORA algorithm for network flow models with improved stability and convergence properties, ASCE J. Hydr. Eng. 127 (5) (2001) 380–391.
[44] M. Oldenburg, K. Pruess, Dispersive transport dynamics in a strongly coupled groundwater-brine flow system, Water Resour. Res. 31 (1995) 289–302.
[45] C. Oltean, M.A. Bués, Coupled groundwater flow and transport in porous media. A conservative or non-conservative form, Transp. Porous Media 44 (2) (2001) 219–246.
[46] G.F. Pinder, H.H. Cooper, A numerical technique for calculating the transient position of the saltwater front, Water Resour. Res. 6 (1970) 875–882.
[47] G. Segol, Classic Groundwater Simulations – Proving and Improving Numerical Models, PTR Prentice-Hall, Englewood Cliffs, 1994.
[48] G. Segol, G.F. Pinder, W.A. Gray, A Galerkin-finite-element technique for calculating the transient position of the saltwater front, Water Resour. Res. 11 (2) (1975) 343–347.
[49] R.K. Senger, G.E. Fogg, Stream functions and equivalent freshwater heads for modelling regional flow of variable-density groundwater 1. Review of theory and verification, Water Resour. Res. 26 (9) (1990) 2089–2096.
[50] D.T. Thorne, C.D. Langevin, M.C. Sukopc, Addition of simultaneous heat and solute transport and variable fluid viscosity to SEAWATER, Comput. Geosci. 32 (2006) 1758–1768, doi:10.1016/j.cageo.2006.04.005.
[51] T. Tucciarelli, D. Termini, Finite-element modelling of floodplain flows, ASCE J. Hydr. Eng. 126 (6) (2000) 416–424.
[52] I. Voss, A finite-element simulation model for saturated–unsaturated fluid-density-dependent groundwater flow with energy transport or chemically-reactive single-species solute transport, in: US Geol. Surv., Water Resour. Invest., Rep. 84-4369, 1984, p. 409.
[53] I. Voss, W.R. Souza, Variable-density flow and solute transport simulation of regional aquifers containing a narrow freshwater–saltwater transition zone, Water. Resour. Res. 23 (10) (1987) 1851–1866.
[54] A. Younes, P. Ackerer, R. Mosè, Modelling variable-density flow and solute transport in porous medium: 2. Re-evaluation of the salt dome flow problem, Transp. Porous Media 35 (3) (1999) 375–394.